Peer-reviewed Statement

Philadelphia and the Schuykill under extreme hydrometeorological events

By Dingyu Xuan, M. Ani Hsieh, Douglas Jerolmack & Hugo N. Ulloa.

Philadelphia and the Schuylkill under extreme hydrometeorological events

D. Xuan[1,2]*, M. A. Hsieh[3,4], D. J. Jerolmack[1,4], and H. N. Ulloa[1]*

[1] Department of Earth and Environmental Science, University of Pennsylvania, USA

[2] Department of Civil and Environmental Engineering, Imperial College London, UK

[3] Department of Computer and Information Science, University of Pennsylvania, USA

[4] Department of Mechanical Engineering and Applied Mechanics, University of Pennsylvania, USA

The Schuylkill River, a lifeline for Philadelphia, faces intensifying stress from urbanization and increasingly severe extreme hydrometeorological events (EHMEs) driven by climate change. Understanding how urban estuarine rivers respond to EHMEs remains challenging due to limited high-resolution data and the complexness of human-modified landscapes. Here, we combine long-term hydrological records, a 1-m resolution urban landscape model, remote sensing, citizen-generated data, and advanced hydrodynamic simulations to examine the Schuylkill River's response to EHMEs, focusing on Hurricane Ida's unprecedented flood on September 1, 2021. Ida triggered the river's highest-ever recorded flow discharge of 3,367.7 m³/s—nearly 100 times its average flow. This unique dataset enabled us to build a comprehensive flood model, capturing the dynamics of urban flooding and its impacts on Philadelphia's population at the street level. Our analysis reveals that past hydrological conditions and

*To whom correspondence should be addressed; E-mail: dyxuan@sas.upenn.edu, ulloa@sas.upenn.edu

high-resolution urban terrain models are essential for accurately resolving water pathways and identifying the most vulnerable populations during EHMEs. Furthermore, we discovered that extreme discharges in the Schuylkill have intensified over the past century, underscoring escalating flood risks for Philadelphia's residents. Our numerical experiments reveal that extremer flow discharges added to high tide conditions, working as a "downstream water gate", can create significant expansions of the flooded area, penetrating through Philadelphia's most densely populated neighborhood. These findings highlight the urgent need for integrated research on EHMEs in urban estuaries worldwide to enhance flood preparedness and resilience.

Introduction

Floods are the most frequent and pervasive hazard among natural disasters. There is around 1.6 billion people vulnerable to 1-in-100-year floods, among which 89% come from low- and middle-income countries[1]. These extreme hydrolometeological events (EHME), including floods and storms, have caused global annual economic losses of $136.7 billion on average between 2003 and 2022[2]. The number has dramatically increased in the 21$^{\text{st}}$ century, surpassing $350 billion in 2024[3], which is more than seven times the amount President Biden allocated for climate resilience and adaptation[4]. In many regions, the harshness of rain-generated floods is expected to worsen due to the intensification of super storms fueled by climate change and widespread urbanization around rivers[5;6;7], which often hinder their natural pathways and lateral expansion towards human-altered floodplains[8]. Furthermore, in the case of tidally influenced rivers, continuous sea level rise and tropical cyclones striking coastal regions more intensively at landfall[9;10] is amplifying the severity of floods and population vulnerability[11;12]. Currently, 13.3% of the population (40.8 million people) in the contiguous United States (CONUS) is vulnerable to a 1-in-100-year flood[13]. Yet, despite broad recognition of flood risks across the CONUS, future trends remain poorly understood, creating uncertainties in local-scale flood management[13;14]—particularly in small catchments[15] and estuarine cities[16;17;18]. The latter is the scenario of many cities settled along the coastline of the Atlantic Ocean and other regions, including Southeast Asia and Europe[19], witnessing the increasing frequency of compound floods owing to forceful rainstorms carried by hurricanes and typhoons[12]. A vivid example is the City of Philadelphia.

Despite its historical legacy, the "Schuylkill (Hidden Creek) River" crossing the City of Philadelphia has long been ignored. However, the recent impact of Hurricane Ida, one of the most destructive and top 6 economic loss disasters in the past two decades[20], serves as a stark reminder of the inherent connection between the city and its iconic river. The remnants of Hurricane Ida, along with seven subsequent tornadoes that swept through Philadelphia between September 1st and 2nd, 2021, resulted in an unprecedented discharge and a devastating flood wave along the Schuylkill River, leaving long-lasting flood damage across the city[21]. Previous research has focused on examining the water quality and availability of the Schuylkill River[22;23;24;25], but there is still a critical gap in understanding the river's dynamics and the potential flood risks within its catchment, which requires urgent investigation and analysis. Addressing these challenges is of utmost importance, especially in the lower, tidally influenced section of the Schuylkill, where the complex and poorly explored interplay between tidal and flood waves[26;27;28;29] may create extreme flow conditions, significantly increasing hazards for the densely populated Center City area and the surrounding neighborhoods. As Hurricane Ida's remnants swept through Philadelphia, the peak discharge of the flood wave in the Schuylkill River coincided with a low yet rising tide, raising the question on how the interaction between flood waves and tides impact the flooding magnitude in urban estuaries such as the Lower Schuylkill River.

While hydrodynamic models enable simulating flood inundation on complex terrains, comprehensive representation and prediction of floods in urban catchments persist as a significant interdisciplinary challenge[30;31]. This is because of the still limited coverage of LiDAR-based high-resolution urban landscape models and access to coherently integrated multidimensional observations to constrain such model[32;33]. Furthermore, several of the broadly used modeling frameworks still lack the ability to efficiently operate multidimensional data and perform accurate, high-fidelity numerical integration of the governing equations[34;35], which impede the robustness of mass and momentum budgets, thus exacerbating the challenge. Nevertheless, high-resolution terrain mapping is continually advancing, leading to the development of digital elevation models that capture cities' intricate landscapes. Combined with integrated, publicly available databases, terrain models unlock new opportunities to gain deeper insights into the dynamics of urban flooding. This allows us to characterize better how storm waters store and flow through metropolitan landscapes, paving the way for an in-depth understanding of this complex phenomenon and its impacts on communities at the human scale.

This study presents a comprehensive analysis of the urbanized Lower Schuylkill watershed under EHME and its impact on surrounding communities, with an intentional focus on Philadelphia's unprecedented flooding caused by the remnants of Hurricane Ida in 2021. We reveal that the severity of compound flood inundation in Philadelphia is significantly exacerbated by urbanization. Specifically, the impervious surfaces of the urban landscape have a dual effect: they increase surface runoff by hindering infiltration, while the city's complex infrastructure acts as a labyrinth, trapping runoff before it reaches major watercourses, ultimately affecting nearby rivers and floodplains. Our findings also highlight the disproportionate impact of Hurricane Ida on the lowest-income population, who suffered the most, emphasizing the urgent need for targeted interventions to protect vulnerable communities. Additionally, we discovered a disturbing trend of shortened return periods for extreme river discharge events over recent decades. Indeed, our model shows that the Schuylkill River's capacity to buffer extreme events without flooding has been reduced to a 100-year return period. Beyond this threshold, the river expands laterally at a logarithmic rate. Lastly, our study underscores tides and rainfalls' significant yet differential influence in shaping the discharge and flooding extent of the Schuylkill River. These critical findings provide guidance for urban planners and policymakers in Philadelphia, and although they might seem uniquely local, the challenges we uncover and tackle here are pervasive across estuarine cities worldwide[36], each with its distinctive scenery and characters.

Scenery and characters

We examine the interplay between three main characters, the City of Philadelphia, the Schuylkill River, and Hurricane Ida, to unveil how urban landscapes connected to estuarine rivers face EHME intensified by climate change. But who is who in this scenario?

Philadelphia

The City of Brotherly Love is the cradle of the United States of America (USA), the keeper of its history, and the heart of the grand metropolitan area of the Mid-Atlantic (Fig. 1A). With a stable 1.5 MM population over the last 50 years, Philadelphia is the sixth most populous city in the USA, a diverse and multicultural university city, which is bordered by the East by the Delaware River and crossed by the Schuylkill River (Fig. 1B).

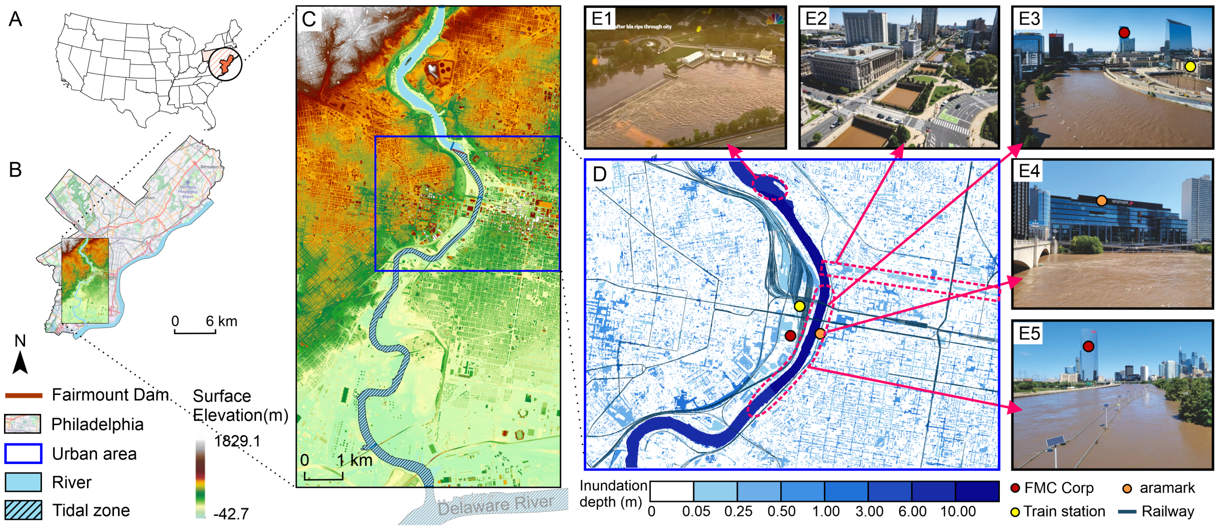

Figure 1: Map of research area and flood inundation of the urban center validated by drone images. (A) The location of Philadelphia in the US. (B) Research area in Philadelphia overlaid with Open Street Map. (C) Surface elevation of the study area. (D) Flood inundation map based on the DSM with railway lines overlaid. (E1 - E5) Drone images with landmarks were collected from the social media, reflecting the real inundated regions.

Schuylkill River

As one of the largest tributaries of the Delaware River, the Schuylkill River has played a vital role in Philadelphia's development for over 300 years[37]. It has provided essential resources such as drinking water, hydro-power, and recreational opportunities while preserving wetlands and wildlife habitats[38]. The Lower Schuylkill, meandering through the urban center of Philadelphia, has been a hub of human activities, with numerous transportation systems, hospitals, and universities along its bank (Fig. 1C). The annual average river discharge, ranging between 25 and 160 m^3/s, has exhibited an upward trend from 1931 to the present (SI Appendix, Fig. S2A). The flow pattern follows a clear seasonal cycle, with higher discharge typically observed in the spring and lower levels in the autumn, suggesting the snowmelt from upstream is likely the primary source of replenishment. However, an increasing number of peak river events have occurred recently during the autumn, driven by the rising frequency of hurricanes due to climate change[39;40] (SI Appendix, Fig. S2B). The Fairmount Dam divides the river into tidal and non-tidal affected zones, further influencing its dynamics (SI Appendix, Fig. S4).

Hurricane Ida

In late August 2021, an initial tropical depression, fueled by warm ocean waters and favorable atmospheric conditions, was formed in the Caribbean Sea[41]. It rapidly intensified into hurricane category and was named Ida, as it moved northwest, reaching Category 4 strength before making landfall in Louisiana on August 29[42]. Ida's strong winds, storm surges, and heavy rainfall caused widespread destruction in the Gulf Coast region, before weakening and moving inland, where it brought severe flooding and tornadoes to parts of the northeastern United States, including Pennsylvania and New York.

Results

Severity of the Flood at the Heart of the City

As many cities crossed by estuarine rivers, the potential flooding severity of Philadelphia is governed by three primary factors: river flow, rainfall within the watershed, and tidal waves that propagate upstream through the estuarine region. We investigate the hydrodynamics of Lower Schuylkill River and its watershed's response to compound flood events utilizing a multidimensional array of in-situ and remote data and the GPU-based numerical framework LISFLOOD-FP (see *Materials and Methods* and Appendix). We first turn our focus on the record-breaking flood resulting from the remnants of Hurricane Ida in late Summer 2021.

To validate the hydrodynamics model's ability to accurately reproduce flooded areas in the floodplain, we used citizen-reported data, drone and satellite images, along with in-situ observations, such as river discharge and surface elevation within the channel (see the

SI Appendix, Table S1). The drone images captured during Ida's flood closely matched the model's results, especially along the east riverbank that links the Schuylkill to Center City. The model successfully reproduces the severe flooding observed in Fairmount Park, near the Philadelphia Museum of Art, Vine Street and the Schuylkill Trail (Fig. 1E1-E5). Our findings confirm that the east riverbank is highly vulnerable to flooding, due to its elevation, channelization of the west bank to protect critical infrastructure, and local geomorphology. This heightened risk is especially pronounced in the middle section of the Lower Schuylkill (Fig. 1D). Furthermore, nearly all railways along the Schuylkill River were affected by flooding. Those on the east bank, located closer to the river, were primarily impacted by overbank flooding, while the west bank was mainly affected by heavy rainfall (Fig. 1E3). The combined effects of river overflow and rainfall create a significant flood hazard, particularly on the east side of the Schuylkill River, extending into the central area of Philadelphia. However, what factors made the rainstorm brought by Hurricane Ida so impactful in Philadelphia? Urbanization and saturated soils may contribute to heightened surface runoff, potentially amplifying flow rates in the Schuylkill River. This prompts us to explore the influence of urbanization and previous hydrological occurrences on the flood inundation triggered by Ida.

Urbanization and Prior Hydrological Processes Shaping Flood Risk

We assess the role of urbanization by performing numerical experiments without and with the urbanized landscape surrounding the Lower Schuylkill River. Inundation maps, showing spatially varying water depths, reveal the most severely impacted areas during Hurricane Ida's event using two landscape elevation models (Fig. 2): Digital Terrain Model (DTM) and Digital Surface Model (DSM) (SI Appendix, text). DTM characterizes the surface elevation without human interference (i.e., a bare land), so the surface runoff can flow naturally from higher to lower elevation, reaching at some point the river channel. In contrast, the DSM-based inundation (Fig. 2B) displays the intricacies of Philadelphia's urban landscape, hindering natural surface runoff flow to the nearby river channel. This results in approximately a 30% increase in inundated areas over the floodplain compared to the DTM-based one. The DSM model captures two significant effects of urbanization well. On the one hand, the river's channelization with levees reduces the possibility of overbank flows, resulting in less river flood inundation in the adjacent dramatically modified floodplains. On the other hand, the blocking effect of those urban infrastructures creates numerous puddles after extreme rainfall, forming stagnant water that hinders the traffic of pedestrians, bicycle riders, and, in extreme conditions, motorized vehicles throughout the city. On top of that, these pools of stagnant water also serve as ideal niches for mosquito-breeding sites, especially during wet seasons, thereby increasing the risk of disease outbreaks afterward[43].

Despite urbanization tends to impermeabilize surfaces, high surface moisture before flood events can saturate the permeable surface area of the watershed and further intensify the flood severity, as more surface runoff is generated when the ground is near saturation. Indeed, several small rainfall events prior to Hurricane Ida helped to pre-saturate the ground (Fig. 2C). By determining the surface runoff coefficient ($\mathcal{C}$), quantifying the proportion of precipitation transformed into surface runoff during a EHME, we can indirectly gain information about the land's capacity for infiltration. The rainfall event characterized by the "peak b" was 37.35% higher than the one of "peak a", despite a lower rainfall intensity before the peak (see Fig. 2C). This implies that a significant portion of the rainfall was either returned to the atmosphere through evapotranspiration or infiltrated into the ground before "peak a", contributing more to subsurface runoff rather than surface flows. In essence, the four-day rain-free interval between these two peaks was insufficient to return the ground to its original "dry state", making the surface more prone to saturation before "peak b" and leading to a greater conversion of rainfall into overland runoff. This indicates that soil moisture saturation or other water storage mechanisms had reached critical levels approximately three days before the extreme flood, significantly heightening the potential severity of the subsequent flooding. Consequently, although the cumulative rainfall before “peak c” was only about 5.5

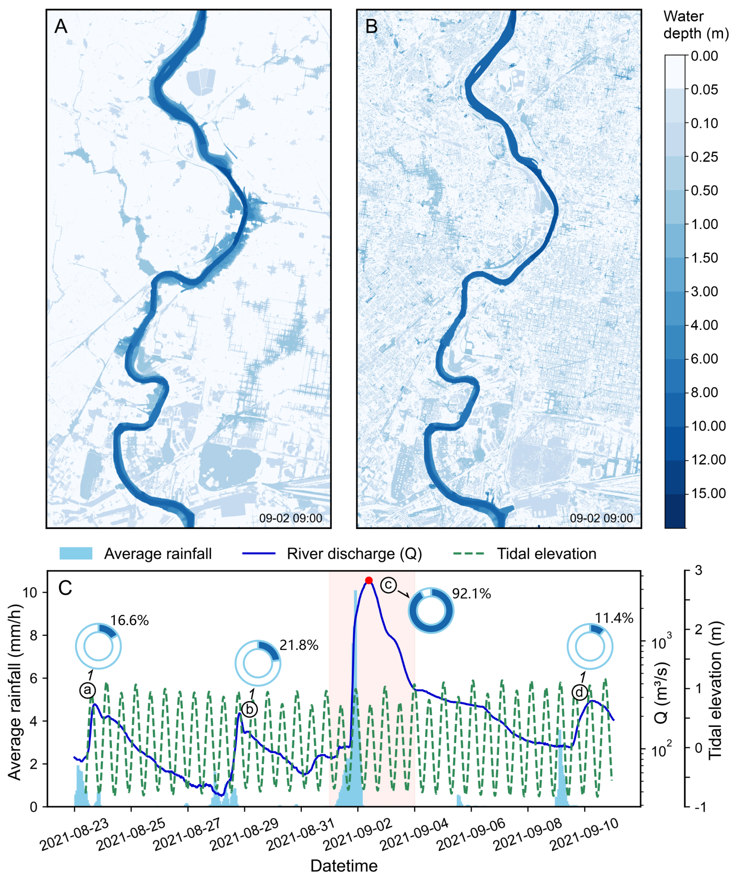

Figure 2: Inundation map resulting from Hurricane Ida utilizing different elevation models. Flood inundation based on DTM (A) and DSM (B) at 9 a.m. on September 2, 2021, shown as the red point in (C). (C) Time series of average rainfall for the whole upstream watershed, river discharge at the upstream boundary condition (BC), and tidal elevation at the downstream BC. The circled letters correspond to four distinct peaks in river discharge, with adjacent doughnut charts illustrating the runoff coefficient. Each complete doughnut chart represents the cumulative rainfall leading up to each peak. In contrast, the blue-shaded portion within each chart depicts the proportion of that rainfall converted into surface runoff. The light orange-shaded area marks the occurrence of the extreme event, which took place between September 1 and September 3, 2021.

times greater than that before "peak b", the surge in river discharge before the "peak c" was 23.2 times higher. This suggested that nearly all the rainfall from this extreme event was converted into surface runoff, as evidenced by the $\mathcal{C}$ of 0.92 at this peak. The river gradually returned to normality around a week after the extreme rainfall, with the $\mathcal{C}$ dropping below 0.12. This analysis highlights the importance of considering prior hydrological processes when modeling EHME.

The fact that urbanization has a major impact on flood inundation distribution raises a fundamental question: Who gets impacted the most during extreme weather events and floods in an urban catchment?

Flood Distribution on Socioeconomic Landscape

We utilized a Socioeconomic Index (SEI), composed of eight factors, to measure flood risks at an individual level. This index reflects the socioeconomic status (SES) and divided the population of our research area into five groups. Aging is the least concerning issue in this watershed, while housing burden, low educational attainment, and racial discrimination are the most dominant issues across nearly all SEI groups (Fig. 3).

The groups with the worst and best SES are identified as the two most vulnerable to extreme floods, each exhibiting inundated percentages exceeding 20%, despite relatively small total inundated areas. This can be explained by inadequate flood preparedness in low-SES regions, where environmental safety is often overlooked[44]. Conversely, high-SES regions experience increased land subsidence and impervious land cover, exacerbating flood risks[45;46]. Additionally, lower-SEI groups in riverine cities tend to reside near rivers to easily access transportation, trade, and scenic views, which increases their susceptibility to flooding. In terms of flood-affected area, the 40-60% SEI group faced the most widespread inundation, reflecting that most census tracts in this watershed fall within this socioeconomic

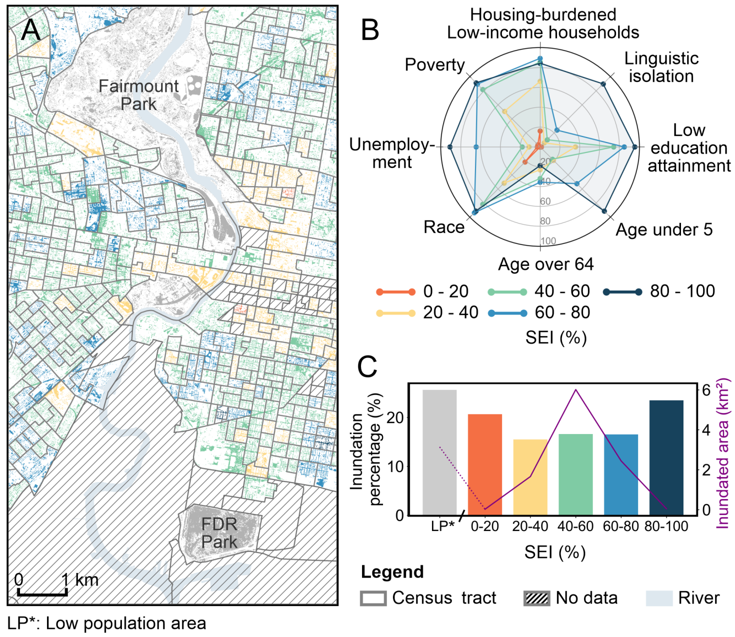

Figure 3: Effect of socioeconomic situation on flood inundation. (A) Inundation in regions with different socioeconomic indices (SEI). Different color indicates different SEI groups, shown in pannel C. (B) Eight components of the SEI and their contributions in different SEI groups. The SEI considered eight socioeconomic problems and was calculated by averaging the values of these components. The values for each component shown in the radar map represent the average values within each SEI group (see *Materials and Methods*). Here, a higher SEI indicates poorer socioeconomic situation. (C) Inundation percentages and areas of different SEI groups for this 2021 flood event. SEI groups exclude the census tract with a population density less than 10 people per square kilometer, showing as the grey region in panel A.

range in Pennsylvania. Apart from areas of concentrated human activity, green spaces like Fairmount Park and FDR Park in Philadelphia serve as natural “sponges”, effectively absorbing and retaining large volumes of water, thereby reducing flood propagation and alleviating downstream impacts. However, during periods of lighter rain followed by extreme rainfalls, these natural sponges may already be saturated, leading to an increase in surface runoff.

Outlook for Future Floods

The Schuylkill River in a changing climate

We investigated the return periods (RPs) of the Schuylkill River over the last century (based on 94 years of historical annual peak flow data), and we discovered that the 2021 inundation has been the most serious fluvial flood event on record. The relationship between RPs and their corresponding peak flows follows a logarithmic trend, which we used to extrapolate more extreme peak flows for higher RPs (Fig. 4A). Yet, delving deeper into the hydrology, the analysis of the Lower Schuylkill River's discharge shows a significant and sustained increase in annual peak over the century. To have a robust statistical representation of this hydrological shift, we performed a frequency analysis for the river discharge every two consecutive decades. Notably, this increase in river discharge for a fixed return period is more observable for higher RPs (Fig. 4B). These previously unreported findings suggest a trend of escalating severe peak discharges during this timeframe and provide direct evidence of the impact of climate change on the hydrological cycle.

We further analyze the relationship between peak flows of different RPs and the river flood inundation area. The result revealed that the 100-year RP serves as a critical threshold in the Center City of Philadelphia, beyond which the flood inundation area increases significantly, following a logarithmic relationship (Fig. 4D). River discharge below this threshold can hardly cause overbank flows without additional precipitation. This phenomenon can be attributed to specific topographical factors: the adjacent river banks, often perpendicular due to urbanization, constrain the river. While beyond the riverbanks, there are many river terraces and human-made infrastructures, such as refuge islands. Higher-RP river flows, which carry greater mass and momentum, are more likely to overtop the banks and surpass these barriers, leading to more extensive flooding (SI Appendix, Fig. S5). This threshold

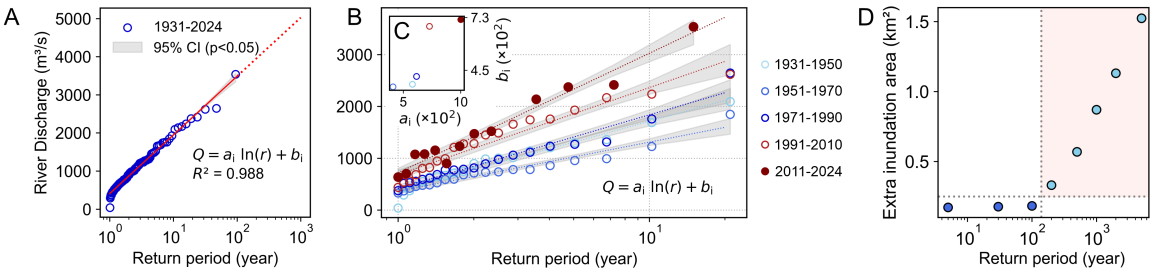

Figure 4: River discharge and flood inundation accross different return periods (RPs). Frequency analysis of river discharge in the Schuylkill River, spanning nearly a century (A) and broken down by every two-decade intervals (B). The return periods were calculated using the annual maxima series method, based on the Weibull plotting position formula (details provided in the SI Appendix , text). The trend lines in both panels were fitted using a logarithmic equation: $Q = a_i \ln(r) + b_i$, where i = 1 to 5 denotes the coefficients for each two-decade period from 1931-1950 to 2011 - 2024 in the panel (B). The fitted coefficients (a_i and b_i) are displayed in panel (C). a_0 and b_0 in panel (A) are 666.9 and 415.6 respectively. The goodness of fit, measured by R_i^2, exceeds 0.93 for all intervals. The gray shaded areas indicate uncertainty zones of the fitting curve at a 95% confidence level. (D) River flood inundation area regarding to each RP except for original water areas, e.g. rivers. The light orange shaded area represents the logarithmic rising range, suggesting that a dangerous threshold for river flood inundation lies above the 100-year RP inflow.

highlights the potential hazard posed by river floods, with peak flows increasing rapidly due to climate change. Moreover, flow intensity has a direct impact on sediment dynamics. Higher river flows have the capacity to locally mine and transport a larger amount of sediments, leading to morphological changes in the river's channel. In the case of the Schuylkill River, we found that when river discharge exceeds 100 m^3/s, sediment concentration shows a linear positive correlation with flow values. However, the relationship between concentration and discharge becomes less distinct when river flow falls below this value (SI Appendix, Fig. S6).

Tidal Effect

The impact of Hurricane Ida's flood wave interacting with a low but rising tide (Fig. 2C) prompts a detailed examination of tidal effects on the estuarine section of the Schuylkill River. Spectral analysis of the downstream surface water elevation over two years (Fig. 5A-B) allowed us to identify and characterize the primary tidal constituents and wave properties. The results reveal that four principal tide constituents primarily influence the Lower Schuylkill: the semidiurnal lunar tides M_2 = 12.42 h, the semidiurnal solar tide S_2 = 12.00 h, and the diurnal tides K_1 = 23.92 h and O_1 = 25.88 h (Fig. 5A, *Materials and Methods*). The interaction between solar and diurnal tides results in a diurnal shift in the timing of maximum and minimum surface water elevation over a fortnightly cycle in the Lower Schuylkill (downstream of the Fairmount Dam), with a period of 14.7 days (SI Appendix, Fig. S7). Additionally, our analysis shows that the annual King tide also impacts the Schuylkill River, occurring typically in July and representing the highest tidal elevation of the year. Furthermore, a harmonic analysis of the tide signal during the extreme flood caused by Hurricane Ida allows for the characterization of the amplitude and phase of the four most energetic tidal constituents (Fig. 5C) during the event. This enables an accurate reconstruction and modeling of the tide dynamics as a function of time during the extreme event (see *Materials and Methods*), thus facilitating the analysis of different tidal-flood wave scenarios.

We investigate the interaction between tides and the river's flood wave by examining how flooding area is affected based on different tidal phases (TP$\in$ $[0, 1]$), which, in this context, represent the time-lag between the tide amplitude of the dominant constituent and the peak in river discharge. The range $0.0 <$ TP ≤ 0.5 is associated with a rising tide amplitude, with TP = 0.5 indicating the phase at which the highest tide amplitude aligns with the peak in river discharge. In contrast, the range $0.5 <$ TP ≤ 1.0 is associated with a

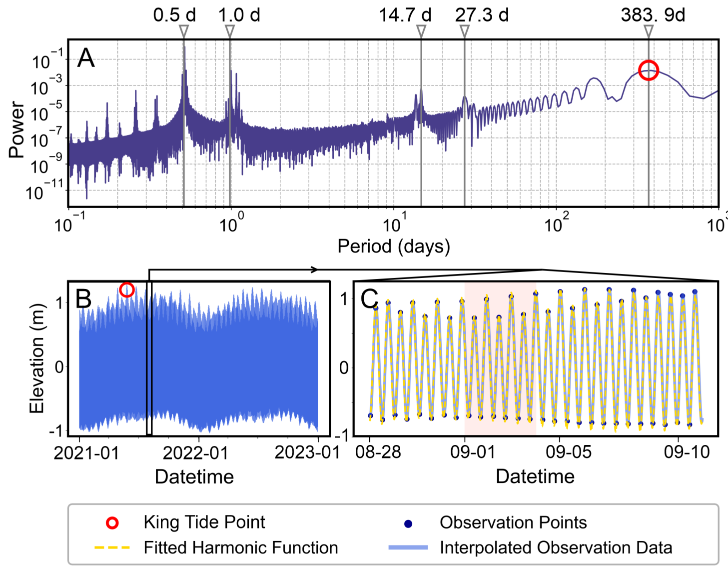

Figure 5: Tidal periods and elevations. (A) Power spectral density analysis using Lomb-Scargle Periodogram: Triangle markers indicate major tidal periods of the Schuylkill River. (B) Observed tidal elevation for two years collected from NOAA tidal stations, reflecting that the King tide here usually happens once a year. The interpolation method “Spline” was used to get a smooth line of the observation. The black rectangle points the tidal elevation during the 2021 flood event. (C) Comparison of tidal observations and harmonic analysis data during the 2021 flood event. NOAA tidal stations in our research areas provided data on the highest and lowest tides, represented by discrete observation points. We applied a “Spline” method to generate a continuous tidal series, and then used the harmonic analysis to fit the data with a root mean square error (RMSE) of 0.084 m. The light orange shaded area marks the occurrence of the extreme event, which took place between September 1 and September 3, 2021.

falling tide amplitude. The elevation for different TPs is selected from the semi-diurnal tide during the peak of the 2021 flood hydrograph (i.e., the tide corresponding to the “peak c” in Fig. 2C). The analysis reveals that the tidal phase severely affects the maximum river flood inundation, with the inundation area positively correlated with the surface elevation of TPs (Fig. 6A, River). The worst-case estuarine scenario is when the river flood wave faces the King tide, as it raises water levels in the Lower Schuylkill and hinders the river’s ability to drain into the Delaware River (Fig. 6A).

To evaluate the impact of tides on compound flood risk, we measured the inundation

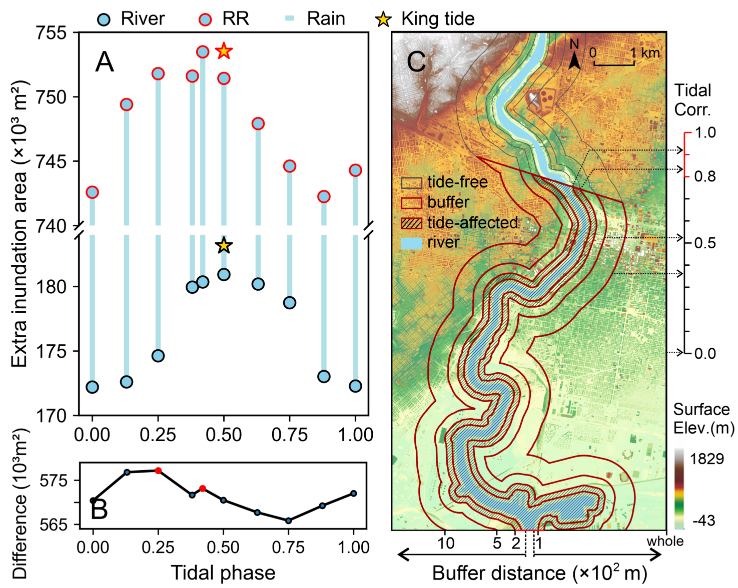

Figure 6: Maximum inundation areas under varying tidal phases and tidally affected regions along the Schuylkill. (A) Inundation areas for 100-year-RP river flood and compound Rain-Riverine (RR) flood. A 100-meter buffer zone along the riverbank was used to calculate the inundation area during RR events. The difference between River and RR flooding indicates the over-bank inundation induced by accumulative rainfall (B). (C) Buffer zones with and without tidal influences for a compound flood event. All buffers were extended along both riverbanks, focusing on regions below the Fairmount dam, where tidal impacts are considered. The tidal impact was determined by analyzing the correlation between the inundation pattern during this compound flood under varying tidal phases and a semi-diurnal signal from the Schuylkill River, using Spearman's rank correlation coefficient (see *Materials and Methods*). The tidal correlation values for buffer zones at distances of 100 m, 200 m, 500 m, 1000 m , and across the whole study area are 0.92, 0.83, 0.53, 0.37, 0.03, respectively. Areas with a tidal correlation exceeding 0.8 are considered tidal-affected, with values over 0.9 indicating strong tidal influence. The base map here is a DSM derived from processed LiDAR point cloud data (see the SI Appendix, text).

area as a function of the tidal phase, incorporating the rainfall pattern cast by Hurricane Ida into our model. Yet, disentangling the effect of tides in the Philadelphia urban landscapes is complicated as surface flow patterns are case specific, complex to predict, and often obstructed by human infrastructure (SI Appendix, Fig. S8). This leads us to the following question: how far can the tide signal penetrate into the city and influence the compound flood event? To address this, we concentrate our analysis into the river and examine the inundation patterns within a buffer zone. Sensitivity analyses show that within a 100-m buffer zone (approximately a block from the riverbank), tides strongly modulate the flood extent for a river discharge of 100-year-RP, with a tidal correlation value exceeding 0.9 (*Materials and Methods*). However, as the buffer distance is further extended, the influences of tides gradually diminished, becoming negligible at around 200 to 250 meters from the riverbank, with the correlation decreasing to around 0.8. Beyond this boundary, rainfall dominates inundation patterns (SI Appendix, Fig. S8) and Fig. 6C).

But how does rainfall affect the flooding in the tidally controlled buffer zone? Our results show that this effect depends on the tidal phase. In fact, tides periodically shrink and enlarge the volume available to absorb both river and rainfall input in the estuarine zone. Therefore, depending on the timing of rainfall and river peaks relative to the tide amplitude, the actual contribution to flooding can vary significantly (Fig. 6A). Fig. 6B illustrates the actual increase in flood area due to rainfall across different tidal phases. We note that during low tide conditions (TP = 0.25), rainfall leads to the largest inundation area within the 100-meter buffer zone. Conversely, during TP = 0.42 (as observed during Hurricane Ida), the near maximum tide amplitude leaves less space for rainfall input to contribute to the buffer zone flooding. In this case, the increase in inundation area is primarily driven by the river peak, which penetrates through Philadelphia's most densely populated neighborhood[47].

Discussion and Conclusions

Flood severity is predominantly driven by the compound effects of hydrologic, atmospheric, and oceanographic elements, with human factors such as urban infrastructure and socioeconomic conditions influencing flood distribution. These combined factors increase the uncertainties in predicting extreme flooding events under climate change. The rising peak river discharge observed annually is direct evidence of how global warming affects the hydrological cycle, highlighting the increasing extremity of river dynamics. We show that for the City of Philadelphia, the river discharge attributed to RPs higher than 100 years causes a logarithmic increase in inundation area. Therefore, small changes in water discharge may flood large urban areas. This threshold is influenced by the geomorphology of the river bank and human interventions (SI Appendix, Fig. S5). Tides, acting as a “downstream water gate”, impede or facilitate river flow depending on the tidal phase (TP), defined based on the time lag between the most persistent tide constituent — semidiurnal M2 tide (Fig. 5A) and the river peak. Thus, the rising tide amplitude, associated with $0.0 < TP \leq 0.5$, inhibits the downstream river flow, whereas the falling tide amplitude for $0.5 < TP \leq 1.0$ streamlines river flow. As river discharge increases, the TP associated with maximum inundation tends to occur earlier, reflecting an earlier balance point between riverine and tidal forces. Yet, the hydrograph typically spans more than a week and incorporates multiple tidal waves and peaks. Since we found that tidal peaks aligning with the rising limb of the hydrograph can lead to higher inundation as river inflow increases, the combined effect of all tidal peaks needs careful consideration when analyzing the entire hydrograph in future studies (SI Appendix, text and Fig. S9).

Flood risk is region-specific, with disadvantaged groups being more vulnerable to high risks[48], and this social inequality is likely to worsen in the aftermath. Flooding can cause significant damage to both social infrastructure and ecosystems while promoting the spread of contagious diseases. During floods, raw sewage leakage can introduce harmful pathogens and chemicals into the environment, increasing infection risks for those directly in contact with polluted water[49;43]. This further exacerbates social disparities, as impoverished regions often lack adequate flood preparedness, sanitation, and vaccination coverage, leaving them vulnerable to natural disasters and disease outbreaks. Although our modeling framework does not include sewage systems, it shows how the city's intricate architecture can promote surface water stagnation in the local low areas within the urban landscape. Not surprisingly, regions with the best socioeconomic conditions still experience severe flooding due to land subsidence and proximity to rivers. However, there is limited research on how floods quantitatively impact long-term socioeconomic issues afterward, including flood-induced unemployment and displacement, loss of access to education, and the resulting mental health problems[44].

Underpinned by recent and rigorous validations, the LISFLOOD-FP model is a powerful framework for accurately simulating flooding resulting from rainfall, river, and tidal forces[50;51;52;53;54]. However, it does have limitations in modeling spatially varying infiltration and accounting for the impact of wind on river hydraulics. With their rapidly changing speed and direction, winds can act as a "water gate" similar to tides. The influences of winds should be carefully considered, as wind-induced waves can affect the average discharge, the bottom shear stress, and the storm surge[35]. Moreover, our study exclude infiltration, assuming the surface was nearly pre-saturated when analyzing the prior hydrological processes. Evaporation was also neglected, as the estimated rate (derived from the revised Penman-Monteith equation[55]) was only about 0.3% of the basal water discharge. This assumption might over-predict flood severity during dry seasons by affecting soil moisture and altering the water storage capability of a catchment. Furthermore, morphological changes in the riverbed were not considered when modeling future scenarios in this paper. These processes can also change flood severity by reshaping river channels, such as altering their width, bathymetry, or roughness, even without changes in river flows[25;56]. Since the available sediment concentration only dates back to 1967-1968, gaining a clearer understanding of the current relationship between sediment dynamics and river flows is essential for predicting how extreme events modify the riverbed and potentially impact the severity of flood inundations.

Hydrological modeling is an essential tool for predicting and managing flood risks, but its accuracy and practicality are often constrained due to limited access to high-resolution data at the building scale, especially in developing countries[57;33]. Rising flooding frequency and severity are drawing increasing attention to flood management policies. Building defenses like dikes and levees is the most common approach to flood protection, especially in coastal cities[35]. However, these engineering solutions often come with substantial maintenance costs due to rising sea levels, may fail under extreme conditions, and can exacerbate flooding risks in nearby regions when implemented without comprehensive planning[58;59;60]. This highlights the need for sustainable and adaptive flood management strategies that account for long-term environmental changes. For example, "hybrid" defenses, combining nature-based solutions and typical "gray" infrastructure, can reduce wave run-up[61]. Local governments should serve as a re-insurer to help reduce premiums and expand insurance coverage[62]. It also has the responsibility to develop systematic evacuation plans ahead of extreme events and raise public awareness, ensuring swift execution of these plans immediately after early warnings are issued[63].

This study elucidates the significance of rainfall, river flow, and tidal influences on the extent and societal implications of flooding resulting from extreme hydrometeorological events within the urban watershed of the estuarine Schuylkill River in Philadelphia. While our findings are particularly relevant to the city of Philadelphia, the challenges identified in relation to the dynamics of compound flooding in urban estuaries are prevalent among estuarine cities globally, each possessing its own unique characteristics and landscapes.

Materials and Methods

Multidimensional Data Collection

LISFLOOD-FP 8.1 hydrodynamic model used in our study can be download from Zenodo (https://zenodo.org/records/6912932). River discharge upstream of the Fairmount Dam, at station PA - 0147500, is obtained from the USGS water database (https://waterdata.usgs.gov/). Tidal elevation downstream is available from a National Oceanic and Atmospheric Administration (NOAA) tide gauge (PA - Station - 8543925 (tidesandcurrents.noaa.gov/). Hourly precipitation grids were provided directly by the Office of Hydrological Development, NOAA. 1-meter Digital terrain model (DTM), named as 3D Elevation Program (3DEP), was available from USGS TNM Service (https://apps.nationalmap.gov/downloader/). Newly released LiDAR point cloud data, used to generate Digital Surface Model (DSM), is available from a Philadelphia LiDAR survey (https://geo.btaa.org/catalog/pasda-7154). River bathymetry data was collected from the latest Lower Schuylkill survey by the US Army Corps of Engineers Philadelphia (https://www.nap.usace.army.mil/Missions/Civil-Works/). Surface landscape is available from National Land Cover Database (NLCD) 2021 (https://www.usgs.gov/). Census tracts 2020, the boundary files of districts and watersheds in Philadelphia can be downloaded from Open Data PHLmaps (https://data-phl.opendata.arcgis.com/datasets/. Demographic data on census-tract level is available from 2017-2021 American Community Survey 5-Year Estimates on U.S. Census Bureau (https://data.census.gov/table/). The latest Environmental justice dataset can be downloaded from PA Department of Environmental Protection (https://gis.dep.pa.gov/PennEnviroScreen/). The Sentinel-2 satellite image is available from Copernicus Browser (https://browser.dataspace.copernicus.eu/). The road network dataset is available from U.S. Census Bureau, Department of Commerce (https://catalog.data.gov/dataset/).

LISFLOOD-FP Model Description

LISFLOOD-FP model is a 1D-2D raster-based hydrodynamic model based on the shallow water equations[64], which enable the modeling of spatially and temporally varying processes like precipitation and local water discharges. We used the state-of-the-art acceleration hydrodynamic solver LISFLOOD-ACC as a local inertial scheme to numerically resolve the water flow throughout a uniform grid describing the landscape, the floodplain, and the river channel[65;66]. This solver has been shown to have high fitting accuracy with real inundations and runs with NVIDIA GPU cores to significantly enhance the computational efficiency[64]. Following[64], we adopt the LISFLOOD-ACC solver, which ignores the advection as it is less critical in friction-dominated floodplain flows but includes the acceleration to reduce chequerboard oscillations during the simulation.

Watershed landscape and friction

The hydraulic resistance encountered by the river flow due to the land surface characteristics and the riverbed's composition is quantified by Manning's frictional coefficient (n). This coefficient exhibits spatial variability and undergoes minor temporal changes. To establish the spatial distribution of the Manning coefficeint within our study area, we have leveraged the United States Geological Survey (USGS) National Land Cover Dataset[67] to analyze the current land use following[68;69;70]. The determined Manning coefficient ranges from 0.027 to 0.160. This detailed mapping of the landscape friction allows capturing the subtle variability in hydraulic resistance across the urban watershed of the Lower Schuylkill River (Fig. S10).

River Discharge Analysis

We conducted the frequency analysis to define return periods of the upstream Schuylkill River by analyzing historical peak discharge from 1931 to 2024. The data before 1990 used the peak of daily average discharge due to the lower temporal resolution during that period, resulting in a slight smoothing of the peak values. Data from 1991 onward utilized peak flow values derived from 30-minute interval measurements. We first sorted the entire dataset in decreasing order. Then, we calculated the exceedance probability by dividing the rank of each peak flow by the total number of years. The return period was determined as the inverse of the exceedance probability. When comparing peak flows over consecutive 20-year periods, the return period was recalculated, as its value is correlated with the length of the dataset.

We used long-time series of river discharges to better understand the single-peaked hydrograph of the Schuylkill River and further design flood hydrographs of more severe scenarios. All hydrographs were then standardised to analyse their shapes (Fig. S11). The time when the river flow peaks is defined as the origin, with time values before and after negative and positive, respectively. The river discharge was scaled to 0 to 1 based on its proportion in the peak flow. The shape of a single-peaked hydrograph of the Schuylkill River is generally similar, so we assumed its shape of a higher RP will almost remain the same. Rainfall intensities and associated river flows tend to flow the Gamma distribution[71]. However, this distribution does not well capture the recession limb of river flows, so exponential functions are commonly used to model the withdrawal of flows[72;73]. Two equations based on the gamma distribution and exponential function, respectively, were used to fit the shape of the hydrograph. The hydrograph for a higher RP is designed by multiplying the fitted function by the calculated peak flow for a given RP based on the 'similar-shape' assumption.

Tidal Analysis

We used the Lomb-Scargle Periodogram Analysis to detect the frequency of periodic signals of the Schuylkill River within the latest two years of tidal elevation data[74]. Our results showed that the Schuylkill River is dominantly tidally modulated by the Lunar (M_2) and the Solar (S_2) semidiurnal tides, and K_1 and O_1 diurnal tide. Thus, we used four Fourier modes to fit and model the tidal elevation signal as a function of time:

$$\eta(t) = \eta_0 + \sum_{i=1}^{4} A_i \sin\left[2\pi\frac{(t+t_0)}{T_i} + \varphi_i\right] \tag{1a}$$

$$t_0 = T_0\,(TP_i - TP_0) \tag{1b}$$

where η_0 = 0.074 m. A_i, T_i, and φ_i are shown in the SI Appendix, Table S1. t_0 is 0 in the real flood case, yet it varies based on different TPs. TP_i represents a different tidal phase, while TP_0, equal to 0.42, is the phase during the real event. T_0 in Eq. 3b is a constant representing the semidiurnal period, approximately equal to 0.5 days.

To quantify the impact of tides on inundation patterns for compound flood events, we used Spearman's correlation coefficient to measure the correlation between the inundation patterns (dataset X) and a semi-diurnal signal of the Schuylkill River (dataset Y). All data in each dataset was ranked in an ascending order. The detailed equation is as followed[75]:

$$r_s = 1 - 6\frac{\sum_i d_i^2}{n(n^2-1)} \tag{2}$$

where n is the number of data in the dataset; d_i is the ranking difference between two datasets. r_s has a value ranging from 0 to 1, with a higher value representing a higher correlation.

Socioeconomics Indices

The SEI is the average value of eight socioeconomic components, which are percentile values calculated for each census tract based on the distribution of all values across Pennsylvania (Penn)[76]. We excluded low-population-density areas when analyzing inundation for different SEI groups to avoid misleadingly favorable SES. The value of the inundation percentage was calculated by dividing the total inundation area in each SEI group by the total census tract areas in the same SEI group.

The socioeconomic statistics were analyzed based on the 2010 census block groups rather than the latest 2020 groups to ensure consistency, as specific components still rely on the 2010 census geometries[76]. However, since the latest demographic data is based on 2020 census block groups, we assumed that the population density within the same census tract remains consistent regardless of location. We then recalculated the population density for these mismatched groups according to their respective area portions. This estimation had minimal impact on detecting low-population areas.

Model Validation

The model was challenged and well-validated through three methods.

Firstly, the overall inundation was qualitatively compared with one Sentinel-2 image, which was the only satellite product with an acceptable cloud cover during this flooding event. We used the water indices AWEIsh[77] to extract the inundation area and set a 15 cm water depth threshold to consider a wet cell[78] and quantify the inundation area. The "Hit rate" for the DTM and DSM modeling results is 0.51 and 0.68, respectively, indicating positive correspondence. This suggests the model adeptly captures the river channel expansion, even though there is a tendency to overpredict the flood severity, particularly in urban areas. This overprediction aligns with expectations since the model excludes infiltration and evapotranspiration.

Secondly, we used the model skill metric (MSM) to assess the modeling performance of the river discharge and surface elevation[79]. The MSMs' results, displayed in Table S2 (SI Appendix), consistently exceed 90%, affirming the model's exceptional ability to reproduce river hydrodynamics accurately.

Lastly, we used drone images with landmarks to compare the actual inundation extent with the model's predictions. This analysis revealed a strong alignment between the observed and modeled inundation areas, indicating the model's accuracy in representing real-world conditions.

Acknowledgments

We greatly acknowledge the support from the U.S. Army Corps of Engineers Philadelphia District for facilitating the sounding survey across the Schuylkill River, the NWS Middle Atlantic River Forecast Center for providing hourly precipitation grids combining rain gauges with radar data, and the support of University of Pennsylvania's URF Award.

The authors declare no competing interests.

Supplementary Information

LISFLOOD-FP Model Description

LISFLOOD-FP serves as the hydraulic engine to resolve rainfall-, topographic-, and tidally-driven hydrodynamics of channel and floodplain flows. It provides a wide range of solvers to deal with flows from different dimensions[80;81;82;83;84;64]. In our study, we used a latest updated numerical solver, acceleration solver (ACC)[64], to simulate river dynamics and map water pathways. This modeling framework will incorporate extensive geographical and weather data, including meteorological, urban, marine, and new underwater observations[25]. The depth-averaged mass and momentum equations for this solver can be written in Cartesian coordinates (x, y, z) as

$$\overbrace{\frac{\partial h}{\partial t} + \frac{\partial q_x}{\partial x} + \frac{\partial q_y}{\partial y} = r,}^{\text{Mass conservation}} \tag{3a}$$

$$\overbrace{\frac{\partial q_x}{\partial t} + \frac{\partial}{\partial x}\left(\frac{q_x^2}{h}\right) + \frac{\partial}{\partial y}\left(\frac{q_x q_y}{h}\right)}^{\text{Rate of change momentum in } x\text{–direction}} = \overbrace{-g\frac{\partial}{\partial x}\left(\frac{h^2}{2}\right) - gh\frac{\partial z}{\partial x} + \frac{g\, n^2 |q_x| q_x}{h^{7/3}},}^{\text{Sum of forces in } x\text{–direction}} \tag{3b}$$

$$\overbrace{\frac{\partial q_y}{\partial t} + \frac{\partial}{\partial x}\left(\frac{q_x q_y}{h}\right) + \frac{\partial}{\partial y}\left(\frac{q_y^2}{h}\right)}^{\text{Rate of change momentum in } y\text{–direction}} = \overbrace{-g\frac{\partial}{\partial y}\left(\frac{h^2}{2}\right) - gh\frac{\partial z}{\partial y} + \frac{g\, n^2 |q_y| q_y}{h^{7/3}},}^{\text{Sum of forces in } y\text{–direction}} \tag{3c}$$

where h is the water depth, t is the time; q_i represents the flow discharge per unit width, with subscript i = x, y in the 3 indicating flow component in the x and y direction. The precipitation rate, r, is treated as a mass flux in 3a, g is the gravitational acceleration, n is the Manning friction coefficient, and z is the landscape elevation coordinate pointing upward. The terms on the left-hand side of 3b and 3c represent the acceleration of the flow caused by the forces acting on the water. The first, second and third terms in the right-hand side of 3b and 3c are the force exerted by the horizontal pressure gradient, the gravity forced and viscous drag force acting in the water, respectively.

The numerical schemes of the solver can handle source and sink terms, enabling the modeling of spatially and temporally varying processes like precipitation and local water discharges. Momentum change results from pressure, gravity, and frictional forces, parameterized with space-dependent Manning coefficients. Unlike many CPU-based solvers, LISFLOOD-FP can run on NVIDIA GPU cores[84;64], significantly enhancing computational efficiency for high-resolution modeling (e.g., 1 meter resolution) that captures flows through narrow city passages. Its robustness and accuracy with real inundations have been demonstrated[85;86].

Watershed Elevation

Surface elevation

This model utilizes an accurate Digital Surface Model (DSM) generated from Light Detection and Ranging (LiDAR) point cloud data collected on March 29, 2022, including dense resolution of the urban landscape surrounding the Schuylkill River (buildings, streets, and canopies). In contrast, the DTM, obtained from 3DEP at one-meter resolution, ignores human-made infraestructures. Both elevation models were adjusted to NAD83 UTM horizontal and NAVD88 vertical datums for consistency. To balance capturing details and computational efficiency, spatial resolution for both landscape models was resampled to 5 m, enough to resolve the flow at the street level. All sinks in both elevation data were filled by ArcGIS to make them hydrologically reasonable and help detect flow directions accurately.

River bathymetry

Accurate riverbed elevation data from bathymetric surveys is crucial for improving the precision of fluvial flood modelling, as microwaves and typical radars on satellites cannot penetrate water[87]. We obtained bathymetric points for the lower Schuylkill River from surveys conducted by the US Army Corps of Engineers, covering both upstream and downstream regions of the Fairmount Dam (see S4). Interpolation methods are employed to create a continuous model of river bathymetry, and the choice of method significantly impacts the robustness of the underwater landscape representation[88;89]. Upstream bathymetric points were distributed along cross-sections, while those around and downstream of the dam were heterogeneously spaced. Based on point distribution and performance tests, we selected the Original Kriging method downstream of the dam for its high accuracy in densely measured areas[88] and the Natural Neighbor method to interpolate observations upstream. Additionally, a "3x3 cells area" low filter window was applied to the DEM to smooth abrupt elevation differences along the flow direction.

Hydrological Analysis

Surface runoff coefficient

The surface runoff coefficient measures the proportion of precipitation that is converted to surface runoff during a hydrological event, reflecting the land's capacity for infiltration and water storage. The detailed equation is provided below:

$$\mathcal{C} = \frac{\triangle \mathrm{Q}}{\mathrm{k\,A}\,(\mathrm{R_{cum}}/\mathrm{R_{cumT}})} \tag{4}$$

where $\triangle$ Q (m^3s^{-1}) indicates the increased in river discharge at each peak; k is a coefficient for unit conversion (here k = 0.278); A (km^2) is the area of the upstream watershed (i.e. 4862.504 km^2); R_{cum} (mm) and R_{cumT} (h) are the cumulative rainfall value and time before each peak, respectively.

Tidal analysis

Local tidal observations only report the highest and lowest surface water levels. We used a Lomb-Scargle periodogram to detect periodic signals in unevenly spaced time series data, which identified the most significant frequencies and corresponding periods in the tide[74].

The four dominant tidal constituents detected by the periodogram were used to be as an initial guess in a harmonic analysis. This analysis helped to fit tidal observation points between August 23, 2021 and September 10, 2021 to get a smooth curve of tidal elevations. The harmonic analysis results exhibit a good fit with the observation data, yielding a root mean square error (RMSE) of 0.084 m.

We focused on river dynamics to assess how tides affect even more extreme events with higher RPs. As upstream flows are intensified to higher RPs, the tidal pattern on river inundation persists, but with an offset in the TP associated with maximum inundation. The shift occurs when the peak tide aligns with the rising limb of the river hydrograph, such as at TP = 0.38 for a 5000-year-RP inflow (Fig. S9A). This is because maximum inundation is reached when downstream tidal forcing balances upstream flows. In the downstream Schuylkill, tides consist of four primary modes. A diurnal tide can alter the semi-diurnal amplitude within its diurnal cycle, so the amplitudes of the peak in adjacent semi-diurnal cycles are different (Fig. S9B). When TP gets smaller, the whole tidal series are shifted rightward visually, allowing the higher-peaking semi-diurnal tide to counter the river's rising limb more effectively. This resistance effect increases with higher river inflows, resulting in a greater river flood inundation. Thus, while peak river flood inundation continues to coincide with the King tide, worst-case scenario should also take the TP into account.

River discharge analysis

A return period (RP) is the reverse of an exceedance probability. The exceedance probability of a river is related to the likelihood that a certain river discharge will be exceeded in any given year. We collected annual peak river flows from 1931 to 2024 and sorted them in a decreasing order, and then defined RPs based on the following equation:

$$P_i = \frac{m}{n+1} \tag{5}$$

where P_i is the exceedance probability for the i-th discharge; m is the rank of the discharge, with the highest value having m = 1; n is the total number of discharge values in the dataset, and "+1" leaves the space for a full probability with a small number of datasets. Here, n = 94. We assumed that the highest value in this 94-year-RP river series closely approximates the 100-year-RP, so we used the latter term in our paper for simplicity. The analyses for every two decades were just the same, but the return period should be re-calculated based on each 20-year time series, which affects the m coefficient in Eq. 5.

We used long time series of river discharge, from 1931 to 2024, to better understand the single-peaked hydrograph of the Schuylkill River, thereby designing flood hydrographs of more severe scenarios. The original hydrographs from observation were shown in Fig. S10A. The 2021 flood event, as simulated above, has a 100-year return period, indicating that this event is the most serious fluvial flood event on record. All hydrographs were then standardised to analyse their shapes (Fig. S10B). Two equations based on the gamma distribution and exponential function were used to fit the rising and recession limb of the hydrograph[73]:

$$Q = \left(\frac{t+t_0}{t_0}\right)^{m-1} \exp\left(-\frac{t(m-1)}{t_0}\right) \tag{6a}$$

$$Q = q_s \exp\left(-\frac{t-t_s}{n}\right) \tag{6b}$$

where Q is the river discharge, t shows the time value, t_0, as a location parameter, is the time duration before peak, m and n are shape parameters, and (t_s, q_s) is the starting point of Eq. 6b. This point is better set at the inflection point of the recession limb rather than just at the peak point, which is the same as what[73] suggested. In this study, t_0 = 25, m = 7.5, n = 11, and the starting point is (8, 0.7). The results were shown in Fig. S10C.

Inundation Analysis

In our study, the calculated inundation areas excluded original water bodies, such as the Schuylkill River at its normal condition. A 15 cm water depth threshold was applied to define a wet cell when rainfall was included in the model, as all cells across the domain contained some water[78].

We further used the model skill metric (MSM) to assess the modeling performance of the river discharge and surface elevation[79]:

$$\mathrm{MSM} = 1 - \frac{\sum |x_m - x_o|^2}{\sum (|x_m - \bar{x}_o| + |x_o - \bar{x}_o|)^2} \tag{7}$$

where x_m is the model result, x_o is the observation data and $\bar{x}_o$ is the average value. MSM close to 1 indicates a better fit between the model and the observation.

Extended Data Table S1: MSM of the river discharge and surface elevation based on DTM and DSM. Locations A1, A2, and B1 are specified in Fig. S1

	River discharge		**Surface elevation**	
	A1	A2	A2	B1
DTM	0.997	0.997	0.921	0.940
DSM	0.997	0.998	0.928	0.948

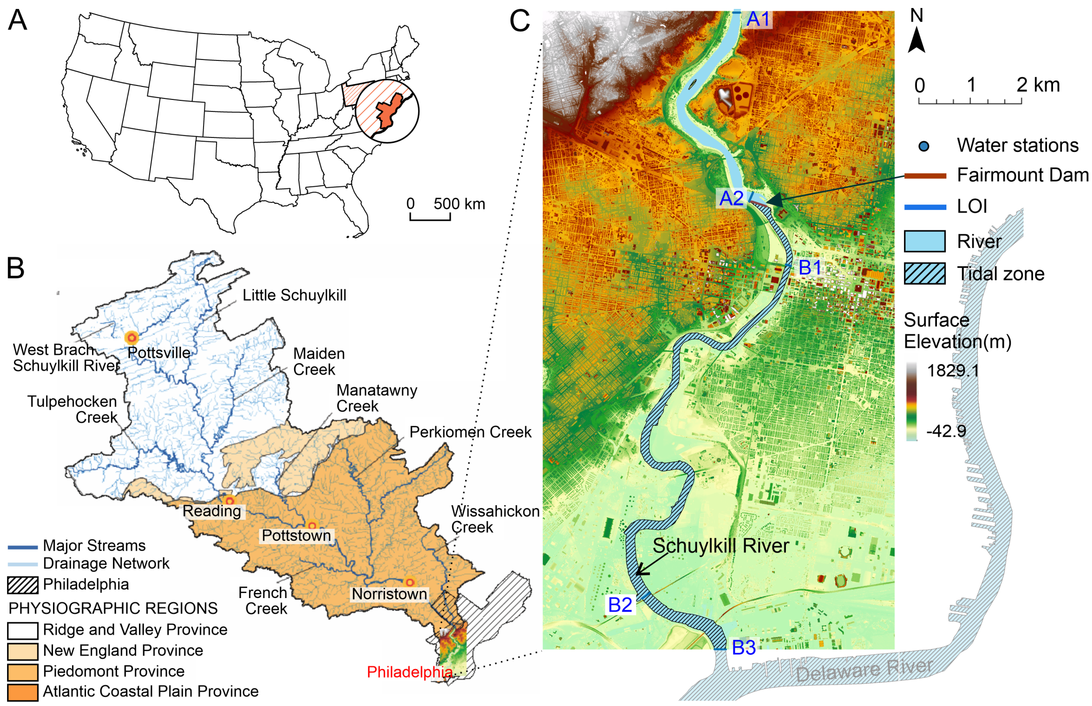

Figure S1: Map of Philadelphia, Schuylkill watershed, and research area. (A) The location of Philadelphia. (B) Physiographic regions of the Schuylkill watershed[38]. (C) Research area and its water stations managed by USGS and NOAA. Five line of interests (LOIs) were used to measure the modelling discharge, with two above the dam (A1, A2) and the rest three below the dam (B1, B2, B3). LOIs were chosen at the modelling boundary or close to water stations. Surface elevation of the study area was collected from a Philadelphia LiDAR survey.

Extended Data Table S2: Detailed parameters of Fourier modes

Tidal components	A_i (m)	T_i (day)	φ_i
1. M_2 (i = 1)	0.892	0.518 (12.422 h)	-1.050
2. S_2 (i = 2)	-0.086	0.500 (12.004 h)	-0.279
3. K_1 (i = 3)	-0.089	0.996 (23.915 h)	-0.277
4. O_1 (i = 4)	-0.065	1.079 (25.886 h)	0.890

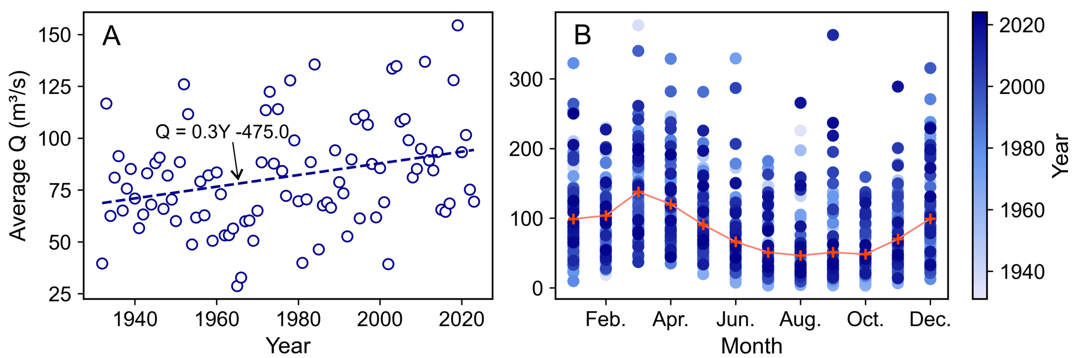

Figure S2: Hydrological regime of Schuylkill River. This figure is adapted from Fig. 1 in[22], with the dataset extended by over 20 years for analyzing the current status. (A) Annual average river discharge of the downstream Schuylkill River from 1932 to 2023. The flow data was collected from USGS gauge station, PA - 01474500. The dash line indicates the overall trend of annual discharge with a positive gradient. (B) Monthly average river discharge at the same station from 1932 to 2023. Red markers show the average flow value within each month.

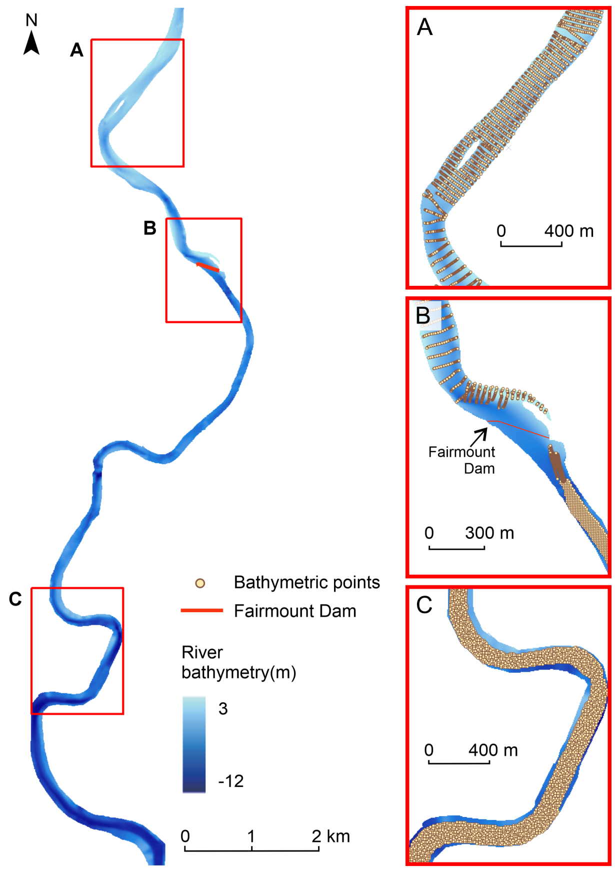

Figure S3: Different spatial patterns of bathymetric points and the river bathymetry after interpolation. (A) Points above the dam, (B) around the dam, and (C) below the dam. The dam serves as a boundary for data collection methods: above the dam, points are collected across river sections, whereas below the dam, they are spaced heterogeneously.

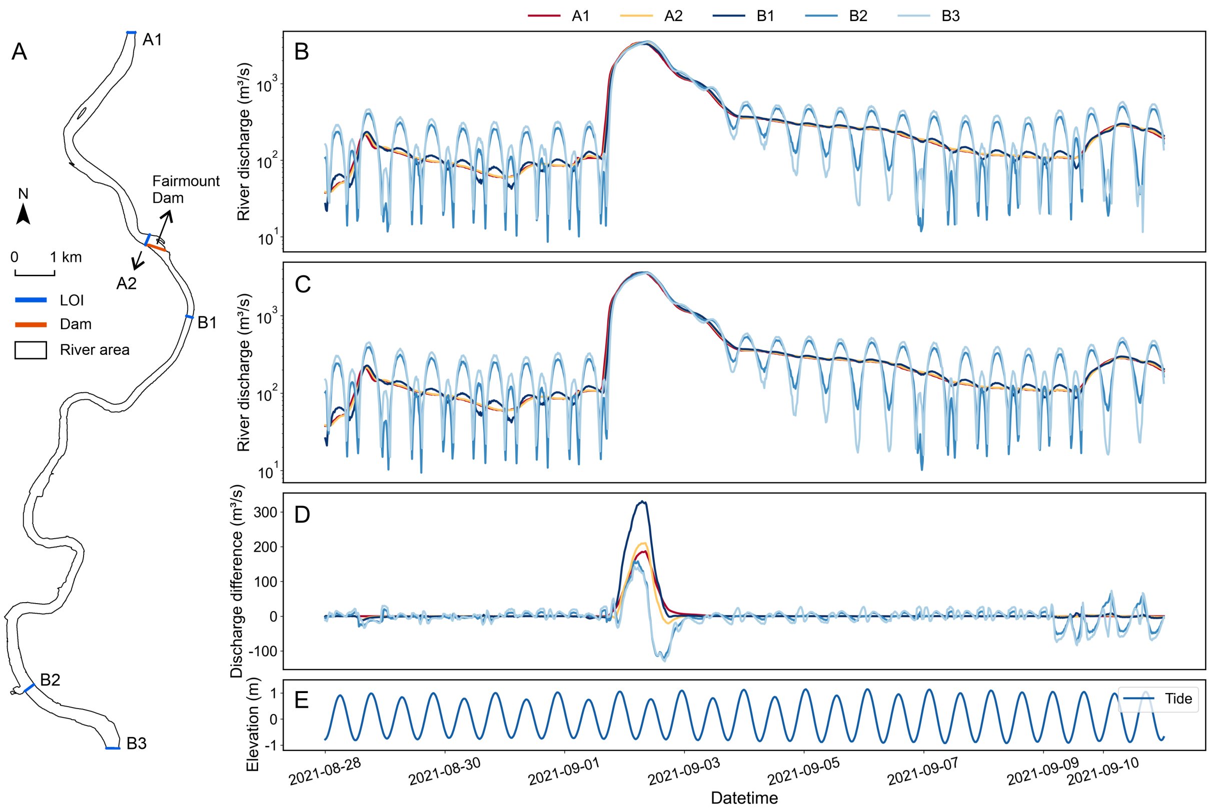

Figure S4: Correlation between river discharge and tides. (A) Five lines of interests (LOIs), same as S1C. LOIs were chosen at the modeling boundary or close to observation stations. (B, C) Output river discharge above and below the dam in the DTM (B) and the DSM (C). (D) The difference in river discharge between DSM and DTM (i.e., DSM - DTM). (E) Tidal elevation at the outlet (B3).

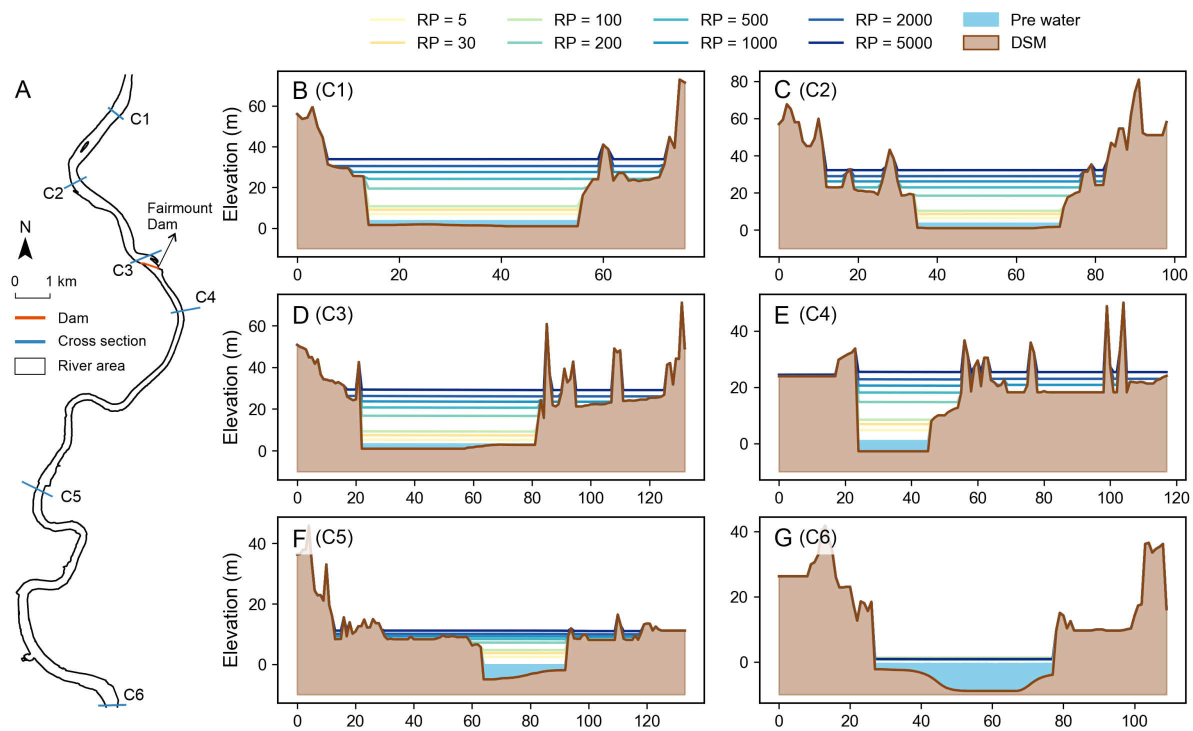

Figure S5: Surface elevation profiles of the Schuylkill River under different return periods. (A) Area profile of the Schuylkill River and six randomly selected cross sections. Three of them are distributed above the dam and the remaining three are below. (B-G) Surface elevation profiles for each cross section from upstream to downstream. The 'Pre water' area represents the initial water level accumulated during the model's spin-up process.

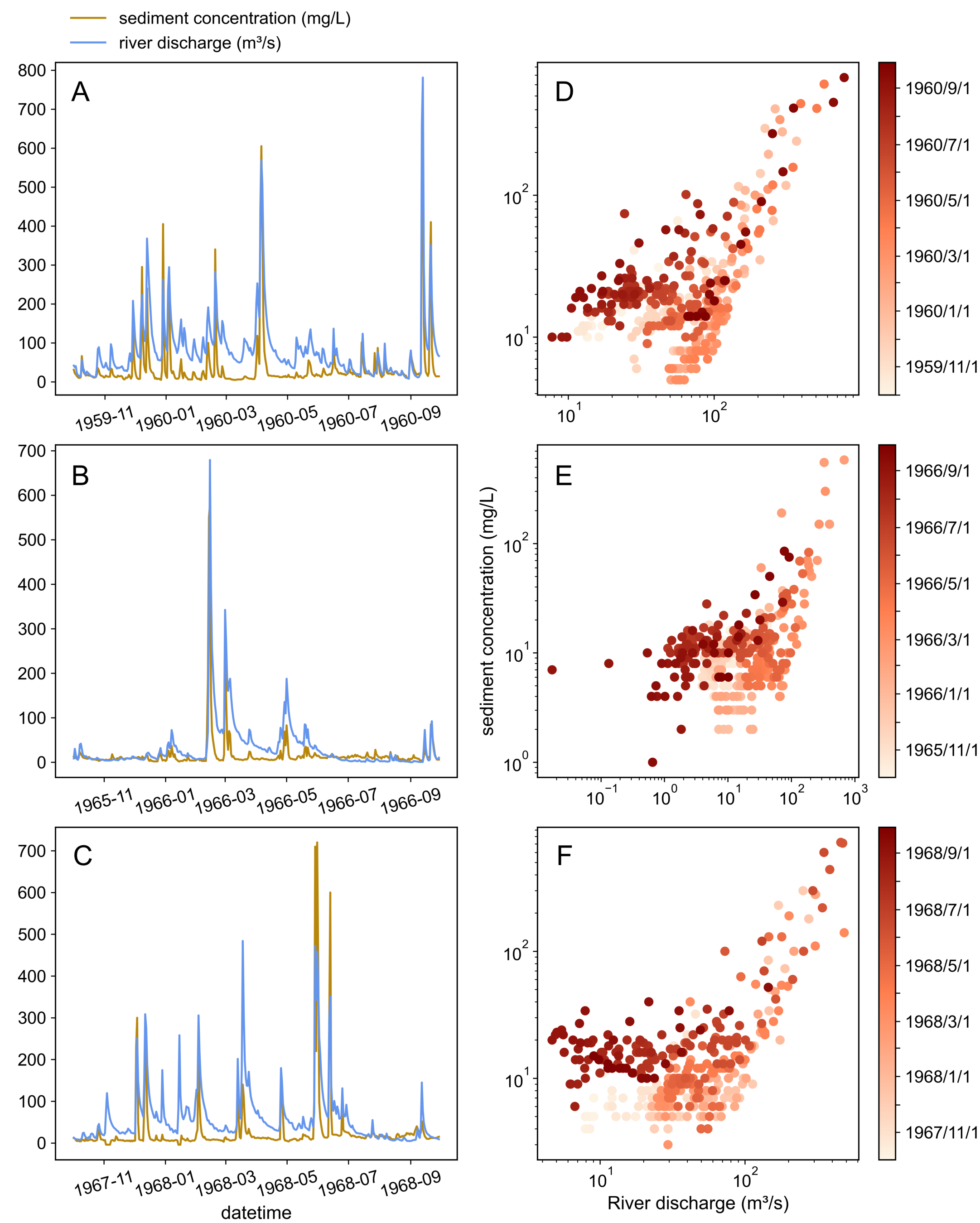

Figure S6: Relationship between sediment concentration and river discharge from 1959 to 1968, based on daily average data collected from USGS. (A-C) Line charts of sediment concentration and river flows across three different periods. The time periods are chosen due to noncontinuous sediment data availability. (D-F) Scatter plots that directly show the correlation between these two factors.

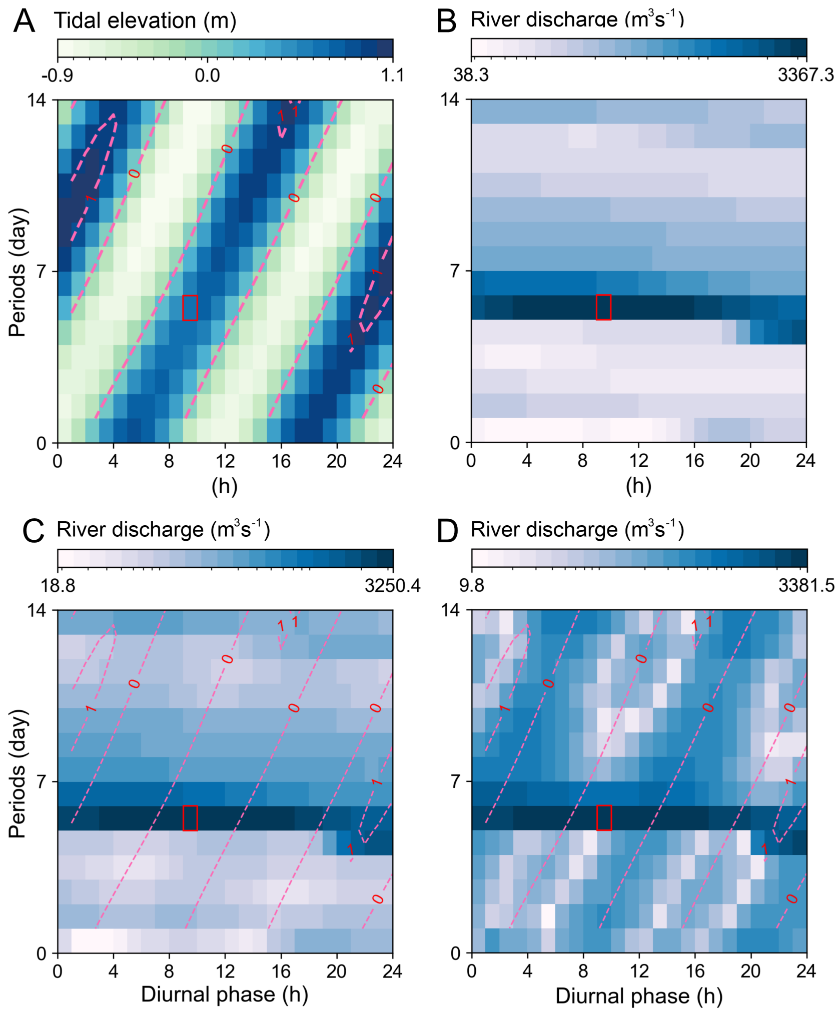

Figure S7: The impact of tides on river discharges based on the urban catchment. (A) Tidal elevation during the modelling period in terms of diurnal phase and fortnightly periods, with the contour overlaid. The red rectangle indicates the time when river discharge peaked. (B) River discharge above the dam (i.e. at A2 in Fig.S3). (C, D) River discharge below the dam with the same contour in (A): (C) at B1; (D) at B3.

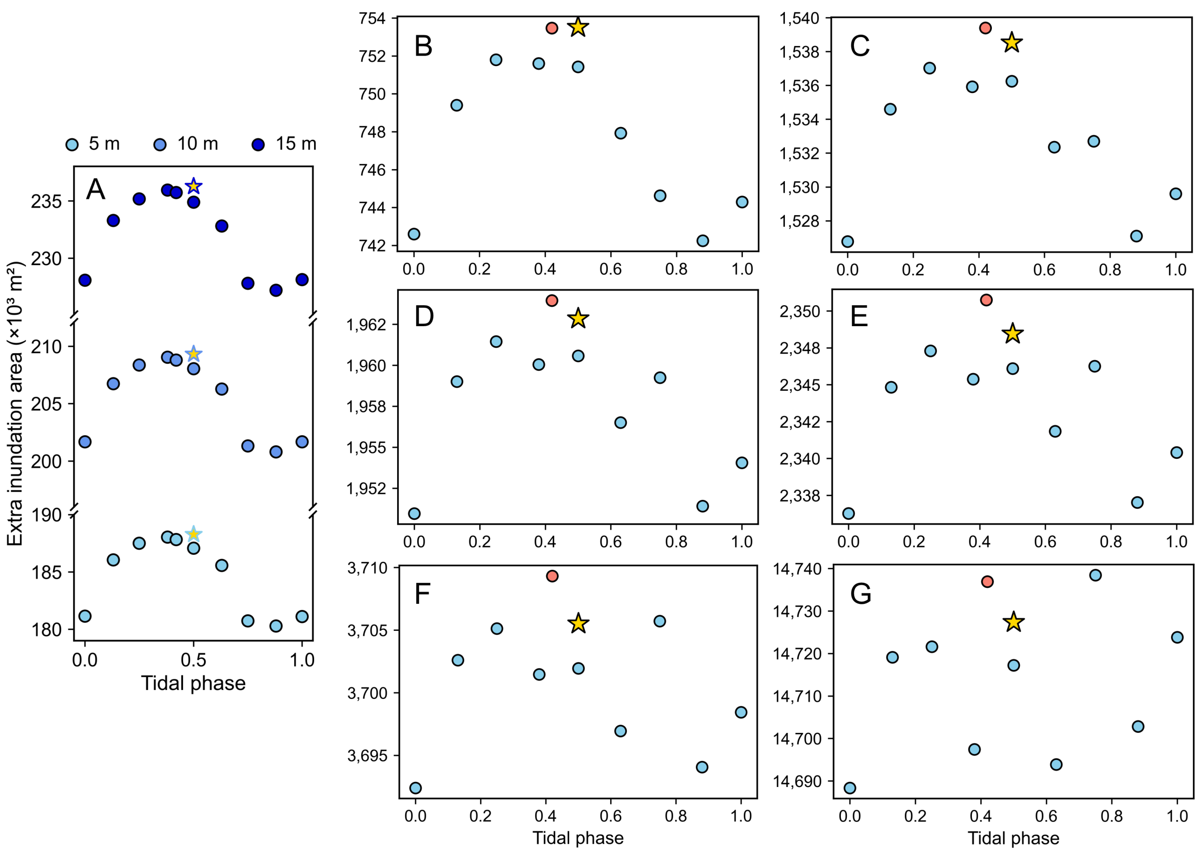

Figure S8: Inundation areas for compound Rain-Riverine (RR) events within different buffer zones under various tidal phases (TPs). (A) Inundation areas within a close distance from the river bank. (B-G) Sensitive analysis between inundation areas and buffer distances: (B) 100 m, (C) 200 m, (D) 250 m, (E) 300 m, (F) 500 m, (G) whole watershed. The red point indicates the tidal phase during this real event, i.e., TP = 0.42. The yellow star is the case facing the King tide, with a predefined TP equal to 0.5.

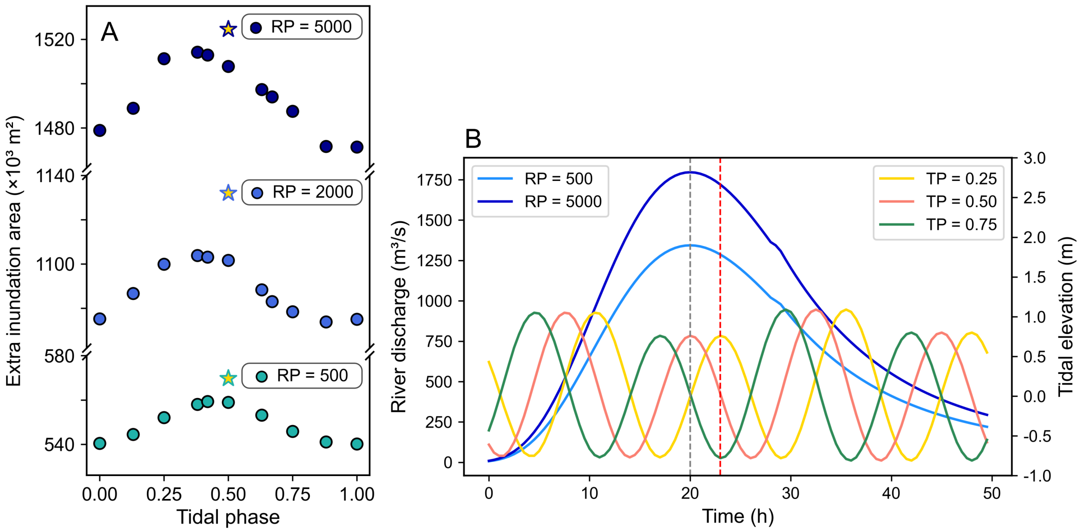

Figure S9: Maximun inundation patterns for larger river inflows under varying tidal phases (TPs). (A) Maximum river flood inundation areas with river inflows at 500-year, 2000-year, and 5000-year return periods (RPs). The yellow stars represent the inundation area facing the King tide. The corresponding RPs are next to the stars. (B) A visual definition of the relationship between different TPs and river peaks. TP = 0.5 is when the tide peak in a semi-diurnal cycle aligns with the river peak. The gray dash line indicates the time when river peaks, while the red one is the time for maximum inundation.

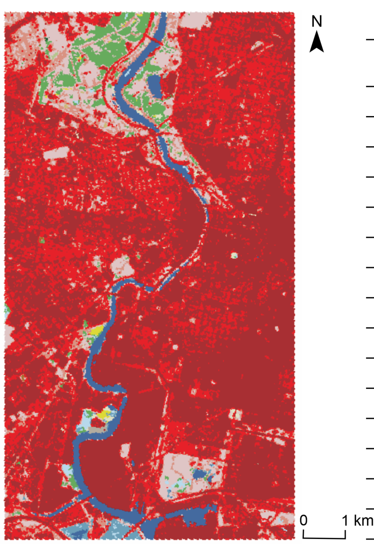

NLCD Topology Value	Description	Manning's Friction (n) Average
11	Open Water	0.038
21	Developed, Open Space	0.040
22	Developed, Low intensity	0.090
23	Developed, Medium Intensity	0.120
24	Developed, High Intensity	0.160
31	Barren Land	0.027
41	Deciduous Forest	0.150
42	Evergreen Forest	0.120
43	Mixed Forest	0.140
52	Shrub/ Scrub	0.115
71/ 72	Herbaceous	0.038
81	Hay/ Pasture	0.038
82	Cultivated Crops	0.035
90	Woody Welands	0.098
95	Emergent Herbaceous Wetlands	0.068

Figure S10: Land use and land cover of the study area and the Manning's friction reference by National Land Cover Dataset[67].

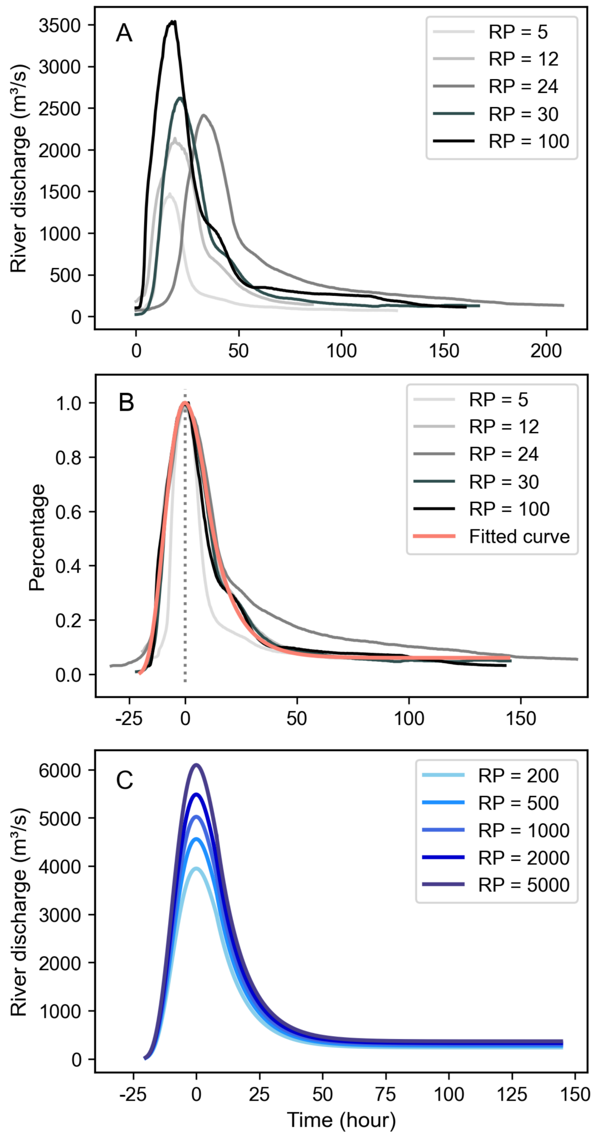

Figure S11: Observed and designed hydrographs at different return periods (RPs). (A) Single-peak hydrographs chosen from historical periods, with RPs of 5, 12, 24, 30, 100 years corresponding to data from 2003, 2020, 2014, 1999, and 2021, respectively. (B) Standardized hydrographs. Peak time is set to 0 and peak value to 1.0, with each flow value represented as a percentage of the peak. A fitted curve here is estimated to be a generalized framework for designing hydrographs. (C) Design-flood hydrographs for higher RPs based on the fitted curve in panel B, with peak flows calculated using the extrapolation equation from Fig.4A in the main text.

References

1. Jun Rentschler, Melda Salhab, and Bramka Arga Jafino. Flood exposure and poverty in 188 countries. *Nature communications*, 13(1):3527, 2022.

2. CRED. 2023 disasters in numbers: A significant year of disaster impact. https://files.emdat.be/reports/2023_EMDAT_report.pdf, 2024. Accessed: 2024-04-05.

3. National Centers for Environmental Information (NOAA). Billion-dollar weather and climate disasters, 2024. Updated: 2024-11-01.

4. Federal Emergency Management Agency (FEMA). President biden announces $1 billion in project selections to make communities more resilient to climate change and natural hazards through his investing in america agenda, 2024. Assessed: 2024-07-02.

5. Hoesung Lee, Katherine Calvin, Dipak Dasgupta, Gerhard Krinner, Aditi Mukherji, Peter Thorne, Christopher Trisos, José Romero, Paulina Aldunce, Ko Barrett, et al. Climate change 2023: synthesis report. contribution of working groups i, ii and iii to the sixth assessment report of the intergovernmental panel on climate change. 2023.

6. James D Miller and Michael Hutchins. The impacts of urbanisation and climate change on urban flooding and urban water quality: A review of the evidence concerning the united kingdom. *Journal of Hydrology: Regional Studies*, 12:345–362, 2017.

7. Wei Zhang, Gabriele Villarini, Gabriel A Vecchi, and James A Smith. Urbanization exacerbated the rainfall and flooding caused by hurricane harvey in houston. *Nature*, 563(7731):384–388, 2018.

8. A Rajib, Q Zheng, CR Lane, HE Golden, JR Christensen, II Isibor, and K Johnson. Human alterations of the global floodplains 1992–2019, sci. data, 10, 1–13, 2023.

9. S Wang and R Toumi. More tropical cyclones are striking coasts with major intensities at landfall. *Scientific reports*, 12(1):5236, 2022.

10. Renzhi Jing, Sam Heft-Neal, Daniel R Chavas, Max Griswold, Zetianyu Wang, Aaron Clark-Ginsberg, Debarati Guha-Sapir, Eran Bendavid, and Zachary Wagner. Global population profile of tropical cyclone exposure from 2002 to 2019. *Nature*, 626(7999):549–554, 2024.

11. Avantika Gori and Ning Lin. Projecting compound flood hazard under climate change with physical models and joint probability methods. *Earth's Future*, 10(12):e2022EF003097, 2022.

12. Mahshid Ghanbari, Mazdak Arabi, Shih-Chieh Kao, Jayantha Obeysekera, and William Sweet. Climate change and changes in compound coastal-riverine flooding hazard along the us coasts. *Earth's Future*, 9(5):e2021EF002055, 2021.

13. Oliver EJ Wing, Paul D Bates, Andrew M Smith, Christopher C Sampson, Kris A Johnson, Joseph Fargione, and Philip Morefield. Estimates of present and future flood risk in the conterminous united states. *Environmental Research Letters*, 13(3):034023, 2018.

14. Louise J Slater and Gabriele Villarini. Recent trends in us flood risk. *Geophysical Research Letters*, 43(24):12–428, 2016.

15. Ashish Sharma, Conrad Wasko, and Dennis P Lettenmaier. If precipitation extremes are increasing, why aren't floods? *Water resources research*, 54(11):8545–8551, 2018.

16. Danial Khojasteh, Steve Hottinger, Stefan Felder, Giovanni De Cesare, Valentin Heimhuber, David J Hanslow, and William Glamore. Estuarine tidal response to sea level rise: The significance of entrance restriction. *Estuarine, Coastal and Shelf Science*, 244:106941, 2020.

17. CL Lopes, MC Sousa, A Ribeiro, H Pereira, JP Pinheiro, L Vaz, and JM Dias. Evaluation of future estuarine floods in a sea level rise context, sci. rep., 12, 8083, 2022.

18. Charlotte Lyddon, Nguyen Chien, Grigorios Vasilopoulos, Michael Ridgill, Sogol Moradian, Agnieszka Olbert, Thomas Coulthard, Andrew Barkwith, and Peter Robins. Thresholds for estuarine compound flooding using a combined hydrodynamic–statistical modelling approach. *Natural Hazards and Earth System Sciences*, 24(3):973–997, 2024.

19. Grey Nearing, Deborah Cohen, Vusumuzi Dube, Martin Gauch, Oren Gilon, Shaun Harrigan, Avinatan Hassidim, Daniel Klotz, Frederik Kratzert, Asher Metzger, et al. Global prediction of extreme floods in ungauged watersheds. *Nature*, 627(8004):559–563, 2024.

20. CRED. 2021 disasters in numbers: Extreme events defining our lives. https://www.cred.be/sites/default/files/2021_EMDAT_report.pdf, 2022. Accessed: 2022-04-29.

21. Maria Pulcinella, Katie Meyer, and Kenny Cooper. Long recovery ahead as ida's remnants lead to historic flooding, tornadoes in philly region, 2021. Accessed: 2021-09-02.

22. Sebastian J Interlandi and Christopher S Crockett. Recent water quality trends in the schuylkill river, pennsylvania, usa: a preliminary assessment of the relative influences

of climate, river discharge and suburban development. *Water research*, 37(8):1737–1748, 2003.

23. Suna Ekin Kali, Achira Amur, Lena K Champlin, Mira S Olson, and Patrick L Gurian. Climate change scenarios reduce water resources in the schuylkill river watershed during the next two decades based on hydrologic modeling in stella. *Water*, 15(20):3666, 2023.

24. Charles A Cravotta III, Daniel J Goode, Michael D Bartles, Dennis W Risser, and Daniel G Galeone. Surface water and groundwater interactions in an extensively mined watershed, upper schuylkill river, pennsylvania, usa. *Hydrological Processes*, 28(10):3574–3601, 2014.

25. Alice K Li, Yue Mao, Sandeep Manjanna, Sixuan Liu, Jasleen Dhanoa, Bharg Mehta, Victoria M Edwards, Fernando Cladera Ojeda, M Ani Hsieh, Maël Le Men, et al. Towards understanding underwater weather events in rivers using autonomous surface vehicles. In *OCEANS 2022, Hampton Roads*, pages 1–8. IEEE, 2022.

26. Haijue Xu, Gang Wang, Zhe Huang, Yaqing Su, Yuchuan Bai, and Jiabo Zhang. Hydrodynamic interactions between tide and runoff in the luanhe estuary in bohai sea, china: From aquaculture reclamation to restoration. *Ocean & Coastal Management*, 239:106586, 2023.

27. PM Orton, FEDERICO ROSARIO Conticello, Francesco Cioffi, TM Hall, N Georgas, Upmanu Lall, AF Blumberg, and K MacManus. Flood hazard assessment from storm tides, rain and sea level rise for a tidal river estuary. *Natural hazards*, 102:729–757, 2020.

28. Yawen Shen, Mohamed M Morsy, Chris Huxley, Navid Tahvildari, and Jonathan L Goodall. Flood risk assessment and increased resilience for coastal urban watersheds under the combined impact of storm tide and heavy rainfall. *Journal of Hydrology*, 579:124159, 2019.

29. Jiun-Huei Jang and Tien-Hao Chang. Flood risk estimation under the compound influence of rainfall and tide. *Journal of Hydrology*, 606:127446, 2022.

30. Elga Salvadore, Jan Bronders, and Okke Batelaan. Hydrological modelling of urbanized catchments: A review and future directions. *Journal of hydrology*, 529:62–81, 2015.

31. Simone Fatichi, Enrique R Vivoni, Fred L Ogden, Valeriy Y Ivanov, Benjamin Mirus, David Gochis, Charles W Downer, Matteo Camporese, Jason H Davison, Brian Ebel, et al. An overview of current applications, challenges, and future trends in distributed process-based models in hydrology. *Journal of Hydrology*, 537:45–60, 2016.

32. Jin Teng, Anthony J Jakeman, Jai Vaze, Barry FW Croke, Dushmanta Dutta, and SJEM Kim. Flood inundation modelling: A review of methods, recent advances and uncertainty analysis. *Environmental modelling & software*, 90:201–216, 2017.

33. Paul Bates. Fundamental limits to flood inundation modelling. *Nature Water*, 1(7):566–567, 2023.

34. Vijendra Kumar, Kul Vaibhav Sharma, Tommaso Caloiero, Darshan J Mehta, and Karan Singh. Comprehensive overview of flood modeling approaches: A review of recent advances. *Hydrology*, 10(7):141, 2023.

35. Keighobad Jafarzadegan, Hamid Moradkhani, Florian Pappenberger, Hamed Moftakhari, Paul Bates, Peyman Abbaszadeh, Reza Marsooli, Celso Ferreira, Hannah L

Cloke, Fred Ogden, et al. Recent advances and new frontiers in riverine and coastal flood modeling. *Reviews of Geophysics*, 61(2):e2022RG000788, 2023.

36. Beatriz Biguino, Ivan D Haigh, João Miguel Dias, and Ana C Brito. Climate change in estuarine systems: Patterns and gaps using a meta-analysis approach. *Science of the Total Environment*, 858:159742, 2023.

37. J. Bennett Nolan. *The Schuylkill*. Schuylkill River National and State Heritage, 2004.

38. Anonymous. State of the schuylkill river watershed. https://schuylkillwaters.org/sites/default/files/State%20of%20the%20Schuylkill.pdf, 2002.

39. Avantika Gori, Ning Lin, Dazhi Xi, and Kerry Emanuel. Tropical cyclone climatology change greatly exacerbates us extreme rainfall–surge hazard. *Nature Climate Change*, 12(2):171–178, 2022.

40. Karthik Balaguru, Wenwei Xu, Chuan-Chieh Chang, L Ruby Leung, David R Judi, Samson M Hagos, Michael F Wehner, James P Kossin, and Mingfang Ting. Increased us coastal hurricane risk under climate change. *Science advances*, 9(14):eadf0259, 2023.

41. Yi-Jie Zhu, Jennifer M Collins, Philip J Klotzbach, and Carl J Schreck III. Hurricane ida (2021): rapid intensification followed by slow inland decay. *Bulletin of the American Meteorological Society*, 103(10):E2354–E2369, 2022.

42. J. L. Beven, A. Hagen, and R. Berg. Tropical cyclone report: Hurricane ida, 2022.

43. John T Watson, Michelle Gayer, and Maire A Connolly. Epidemics after natural disasters. *Emerging infectious diseases*, 13(1):1, 2007.

44. Miyuki Hino and Earthea Nance. Five ways to ensure flood-risk research helps the most vulnerable. *Nature*, 595(7865):27–29, 2021.

45. Leonard O Ohenhen, Manoochehr Shirzaei, Chandrakanta Ojha, Sonam F Sherpa, and Robert J Nicholls. Disappearing cities on us coasts. *Nature*, 627(8002):108–115, 2024.

46. Cheryl Tay, Eric O Lindsey, Shi Tong Chin, Jamie W McCaughey, David Bekaert, Michele Nguyen, Hook Hua, Gerald Manipon, Mohammed Karim, Benjamin P Horton, et al. Sea-level rise from land subsidence in major coastal cities. *Nature Sustainability*, 5(12):1049–1057, 2022.

47. Statistical Atlas, United States Census Bureau. Map of population by tract in philadelphia county. https://statisticalatlas.com/county/Pennsylvania/Philadelphia-County/Population, 2018. Accessed: 2023-May-01.

48. Paul Bates. Uneven burden of urban flooding. *Nature Sustainability*, 6(1):9–10, 2023.

49. Andrea J Linscott. Natural disasters—a microbe's paradise. *Clinical Microbiology Newsletter*, 29(8):57–62, 2007.

50. Sanaz Moghim, Mohammad Ahmadi Gharehtoragh, and Ammar Safaie. Performance of the flood models in different topographies. *Journal of Hydrology*, 620:129446, 2023.

51. Paul D Bates, Niall Quinn, Christopher Sampson, Andrew Smith, Oliver Wing, Jeison Sosa, James Savage, Gaia Olcese, Jeff Neal, Guy Schumann, et al. Combined modeling of us fluvial, pluvial, and coastal flood hazard under current and future climates. *Water Resources Research*, 57(2):e2020WR028673, 2021.

52. Adnan Rajib, Zhu Liu, Venkatesh Merwade, Ahmad A Tavakoly, and Michael L Follum. Towards a large-scale locally relevant flood inundation modeling framework using swat and lisflood-fp. *Journal of Hydrology*, 581:124406, 2020.

53. Iuliia Shustikova, Alessio Domeneghetti, Jeffrey C Neal, Paul Bates, and Attilio Castellarin. Comparing 2d capabilities of hec-ras and lisflood-fp on complex topography. *Hydrological Sciences Journal*, 64(14):1769–1782, 2019.

54. Xushu Wu, Zhaoli Wang, Shenglian Guo, Chengguang Lai, and Xiaohong Chen. A simplified approach for flood modeling in urban environments. *Hydrology Research*, 49(6):1804–1816, 2018.

55. Kaighin A McColl. Practical and theoretical benefits of an alternative to the penman-monteith evapotranspiration equation. *Water Resources Research*, 56(6):e2020WR027106, 2020.

56. Louise J Slater, Michael Bliss Singer, and James W Kirchner. Hydrologic versus geomorphic drivers of trends in flood hazard. *Geophysical Research Letters*, 42(2):370–376, 2015.

57. UC Nkwunonwo, M Whitworth, and B Baily. A review of the current status of flood modelling for urban flood risk management in the developing countries. *Scientific African*, 7:e00269, 2020.

58. Jochen Hinkel, Daniel Lincke, Athanasios T Vafeidis, Mahé Perrette, Robert James Nicholls, Richard SJ Tol, Ben Marzeion, Xavier Fettweis, Cezar Ionescu, and Anders Levermann. Coastal flood damage and adaptation costs under 21st century sea-level rise. *Proceedings of the National Academy of Sciences*, 111(9):3292–3297, 2014.

59. Michelle A Hummel, Robert Griffin, Katie Arkema, and Anne D Guerry. Economic evaluation of sea-level rise adaptation strongly influenced by hydrodynamic feedbacks. *Proceedings of the National Academy of Sciences*, 118(29):e2025961118, 2021.

60. Jonathan WF Remo, Megan Carlson, and Nicholas Pinter. Hydraulic and flood-loss modeling of levee, floodplain, and river management strategies, middle mississippi river, usa. *Natural hazards*, 61:551–575, 2012.

61. Brenden Jongman. Effective adaptation to rising flood risk. *Nature communications*, 9(1):1986, 2018.

62. Jeroen CJH Aerts, Paul D Bates, WJ Wouter Botzen, Jens de Bruijn, Jim W Hall, Bart van den Hurk, Heidi Kreibich, Bruno Merz, Sanne Muis, Jaroslav Mysiak, et al. Exploring the limits and gaps of flood adaptation. *Nature Water*, pages 1–10, 2024.

63. Bokjin Ro and Gregg Garfin. Building urban flood resilience through institutional adaptive capacity: A case study of seoul, south korea. *International Journal of Disaster Risk Reduction*, 85:103474, 2023.

64. Mohammad Kazem Sharifian, Georges Kesserwani, Alovya Ahmed Chowdhury, Jeffrey Neal, and Paul Bates. Lisflood-fp 8.1: new gpu-accelerated solvers for faster fluvial/pluvial flood simulations. *Geoscientific Model Development*, 16(9):2391–2413, 2023.

65. Leanne Archer, Jeffrey Neal, Paul Bates, Emily Vosper, Dereka Carroll, Jeison Sosa, and Daniel Mitchell. Current and future rainfall-driven flood risk from hurricanes in puerto rico under 1.5°c and 2°c climate change. *EGUsphere*, 2023:1–32, 2023.

66. Simbidzayi Hatchard, Rafael JP Schmitt, Francesca Pianosi, James Savage, and Paul

Bates. Strategic siting and design of dams minimizes impacts on seasonal floodplain inundation. *Environmental Research Letters*, 2023.

67. USGS. National land cover database. https://www.usgs.gov/centers/eros/science/national-land-cover-database, 2021. Accessed: 2023-May-01.

68. Mohamed Soliman, Mohamed M Morsy, and Hany G Radwan. Assessment of implementing land use/land cover lulc 2020-esri global maps in 2d flood modeling application. *Water*, 14(23):3963, 2022.

69. Narayan Nyaupane. *Statistical Evaluation of Hydrological Extremes on Stormwater Systems*. Southern Illinois University at Carbondale, 2018.

70. LLC Krest Engineers. Manning's n (roughness coefficient) for hec-ras 2d modeling. https://rashms.com/blog/mannings-n-roughness-coefficient-for-hec-ras-2d-modeling/, 2021. Accessed: 2021-Jan-10.

71. Cristian Martinez-Villalobos and J David Neelin. Why do precipitation intensities tend to follow gamma distributions? *Journal of the Atmospheric Sciences*, 76(11):3611–3631, 2019.

72. Wiesław Gądek, Beata Baziak, Tamara Tokarczyk, and Wiwiana Szalińska. A novel method of design flood hydrographs estimation for flood hazard mapping. *Water*, 14(12):1856, 2022.

73. Monomoy Goswami. Generating design flood hydrographs by parameterizing the characteristic flood hydrograph at a site using only flow data. *Hydrological Sciences Journal*, 67(16):2505–2523, 2022.

74. Jacob T VanderPlas. Understanding the lomb–scargle periodogram. *The Astrophysical Journal Supplement Series*, 236(1):16, 2018.

75. Khawla Ali Abd Al-Hameed. Spearman's correlation coefficient in statistical analysis. *International Journal of Nonlinear Analysis and Applications*, 13(1):3249–3255, 2022.

76. Environmental Justice Office. Pennsylvania environmental justice mapping and screening tool (pennenviroscreen) methodology documentation 2023. https://files.dep.state.pa.us/PublicParticipation/Office%20of%20Environmental%20Advocacy/EnvAdvocacyPortalFiles/2023/015-0501-003-InterimFinal.pdf, 2023. Accessed: 2023-08-15.

77. Xiucheng Yang, Qiming Qin, Pierre Grussenmeyer, and Mathieu Koehl. Urban surface water body detection with suppressed built-up noise based on water indices from sentinel-2 msi imagery. *Remote sensing of environment*, 219:259–270, 2018.

78. Oliver EJ Wing, Paul D Bates, Christopher C Sampson, Andrew M Smith, Kris A Johnson, and Tyler A Erickson. Validation of a 30 m resolution flood hazard model of the conterminous u nited s tates. *Water Resources Research*, 53(9):7968–7986, 2017.

79. Cort J Willmott. On the validation of models. *Physical geography*, 2(2):184–194, 1981.

80. Paul D Bates and APJ De Roo. A simple raster-based model for flood inundation simulation. *Journal of hydrology*, 236(1-2):54–77, 2000.

81. Mark A Trigg, Matthew D Wilson, Paul D Bates, Matthew S Horritt, Douglas E Alsdorf, Bruce R Forsberg, and Maria C Vega. Amazon flood wave hydraulics. *Journal of Hydrology*, 374(1-2):92–105, 2009.

82. Jeffrey Neal, Guy Schumann, and Paul Bates. A subgrid channel model for simulating river hydraulics and floodplain inundation over large and data sparse areas. *Water Resources Research*, 48(11), 2012.

83. Paul D Bates, Matthew S Horritt, and Timothy J Fewtrell. A simple inertial formulation of the shallow water equations for efficient two-dimensional flood inundation modelling. *Journal of hydrology*, 387(1-2):33–45, 2010.

84. James Shaw, Georges Kesserwani, Jeffrey Neal, Paul Bates, and Mohammad Kazem Sharifian. Lisflood-fp 8.0: the new discontinuous galerkin shallow-water solver for multi-core cpus and gpus. *Geoscientific Model Development*, 14(6):3577–3602, 2021.

85. Youtong Rong, Paul Bates, and Jeffrey Neal. Gpu-accelerated urban flood modeling using a nonuniform structured grid and a super grid scale river channel. *Water Resources Research*, 60(6):e2023WR036128, 2024.

86. Leanne Archer, Jeffrey Neal, Paul Bates, Emily Vosper, Dereka Carroll, Jeison Sosa, and Daniel Mitchell. Current and future rainfall-driven flood risk from hurricanes in puerto rico under 1.5 and 2 c climate change. *Natural Hazards and Earth System Sciences*, 24(2):375–396, 2024.

87. L Mullen and PR Herczfeld. Application of radar technology to aerial lidar systems. In *1994 IEEE MTT-S International Microwave Symposium Digest (Cat. No. 94CH3389-4)*, pages 175–178. IEEE, 1994.

88. Chia-Yu Wu, Joann Mossa, Liang Mao, and Mohammad Almulla. Comparison of different spatial interpolation methods for historical hydrographic data of the lowermost mississippi river. *Annals of GIS*, 25(2):133–151, 2019.

89. Venkatesh Merwade. Effect of spatial trends on interpolation of river bathymetry. *Journal of Hydrology*, 371(1-4):169–181, 2009.